Investigating early-type galaxy evolution with a multiwavelength approach ⋆

II. The UV structure of 11 galaxies with *Swift*-UVOT

R. Rampazzo[1], P. Mazzei[1], A. Marino[1], M. Uslenghi[2], G. Trinchieri[3], A. Wolter[3]

[1] INAF Osservatorio Astronomico di Padova, Vicolo dell'Osservatorio 5, 35122 Padova, Italy
   e-mail: `roberto.rampazzo@oapd.inaf.it`
[2] INAF-IASF, via E. Bassini 15, 20133 Milano, Italy
[3] INAF Osservatorio Astronomico di Brera, Via Brera 28, 20121 Milano, Italy

ABSTRACT

Context. GALEX detected a significant fraction of early-type galaxies, in particular S0s, showing Far-UV bright structures, sometimes involving an entire galaxy out to its outskirts. These features suggest the presence of either recent, ongoing and/or prolonged star formation episodes, shedding new light on the evolution of these systems.
Aims. We aim at understanding the evolutionary path[s] of these early-type galaxies and the mechanisms at the origin of their UV-bright structures. We investigate with a multiλ approach the link between the inner and the outer galaxy regions of a set of eleven early-type galaxies selected because of their nearly passive stage of evolution in the nuclear region.
Methods. This paper, second of a series, focuses on the information coming from the comparison between UV features detected by *Swift*-UVOT, tracing recent star formation, and the galaxy optical structure mapping older stellar populations. We performed a surface photometric study of these early-type galaxies, observed with *Swift*-UVOT UV filters, W2 2030Å λ_0, M2 2231Å λ_0, W1 2634Å λ_0, and UBV bands. BVRI photometry from other sources in the literature is also used. Our integrated magnitude measurements have been analyzed and compared with corresponding values in the literature. We characterize the overall galaxy structure best fitting the UV and optical luminosity profiles using a single Sérsic law.
Results. NGC 1366, NGC 1426, NGC 3818, NGC 3962 and NGC 7192 show featureless luminosity profiles. Excluding NGC 1366 which has a clear edge-on disk ($n \approx 1 - 2$), and NGC 3818, the remaining three have Sérsic's indices $n \approx 3 - 4$ in optical and a lower index in the UV. Bright ring/arm-like structures are revealed by UV images and luminosity profiles of NGC 1415, NGC 1533, NGC 1543, NGC 2685, NGC 2974 and IC 2006. The ring/arm-like structures are different from galaxy to galaxy. Sérsic indices of UV profiles for those galaxies are in the range $n = 1.5 - 3$ both in S0s and in galaxies classified as "bona fide" ellipticals, such as NGC 2974 and IC 2006. We notice that in our sample optical Sérsic indices are usually larger than in the UV ones. (*M2*-V) color profiles are bluer in ring/arm-like structures with respect to the galaxy body.
Conclusions. The lower values of Sersic's indices in the UV bands with respect to optical ones, suggesting the presence of a disk, point out that the role of the dissipation cannot be neglected in recent evolutionary phases of these early-type galaxies.

Key words. Galaxies: elliptical and lenticular, cD – Galaxies: individuals: NGC 1366, NGC 1415, NGC 1426, NGC 1533, NGC 1543, NGC 2685, NGC 2974, NGC 3818, NGC 3962, NGC 7162, IC 2006 – Galaxies: fundamental parameters – ultraviolet: galaxies – Galaxies: evolution

1. Introduction

The combination of the Far-UV view provided by *GAlaxy Evolution EXplorer* (*GALEX* hereafter) (Martin et al. 2005) with the Sloan Digital Sky Survey (SDSS hereafter) (Stoughton et al. 2002) has greatly undermined the classical view of early-type galaxies (Es+S0s=ETGs hereafter) as passively evolving galaxies. Statistical studies (e.g. Kaviraj et al. 2007; Schawinski et al. 2007) found that about 30% of massive ETGs show recent/ongoing star formation, with the largest incidence in galaxies located in low density environments. Only a small percentage of cluster ETGs, ~5/9%, shows the classical UV up-turn due to evolved, rising-branch stars whereas ~27/43% shows recent star formation (Yi et al. 2011; Hernández-Pérez & Bruzual 2014, respectively).

In color magnitude diagrams, built with SDSS and *GALEX* magnitudes, galaxies in clusters show a strong morphological segregation: Spirals lie in the blue cloud while ETGs are mainly located in the red sequence (e.g. Yi et al. 2005; Wyder et al. 2007). However, an intermediate area, called "Green Valley", exists, irrespective of the environment. Recently, Mazzei et al. (2014a) provided a description of the galaxy photometric and morphological evolution in the ($NUV - r$) *vs.* M_r color magnitude diagram (CMD) plane applying a SPH code with chemo-photometric implementation to ETGs in the LeoII cloud. Major merging as well as galaxy-galaxy interaction are the mechanisms required to match the global properties of such ETGs. The simulations show that these galaxies spend between 3 to 5 Gyr, depending on their luminosity, crossing the Green Valley before they reach the red sequence and that rejuvenation episodes are more frequent in the less massive ETGs.

GALEX revealed that ETGs with signatures of recent accretion episodes, like shell structures, may have a "rejuvenated" nu-

Table 1. General properties of the sample

Galaxy ident.	Morpho. RSA	Type	M_K	ϵ	PA [deg]	D [Mpc]	M(HI) $10^9 M_\odot$	Group name	ρ_{xyz} [gal Mpc^{-3}]
NGC 1366	S0$_1$(8)	-2.3±0.7	-22.59	0.54	3.8	21.1±2.1	< 1.0	Fornax Eridanus Cloud	0.16
NGC 1415	Sa/SBa late	0.5 ±1.3	-23.47	0.59	141.2	22.7±1.5	0.9	"	0.80
NGC 1426	E4	-4.8±0.5	-23.22	0.32	112.5	24.1±2.4	...	"	0.66
NGC 1533	SB0$_2$(2)/SBa	-2.5±0.6	-23.97	0.37	148.9	21.4±2.1	7.4^a	Dorado cloud	0.89
NGC 1543	RSB0$_{2/3}$(0)/a	-2.0 ±0.8	-24.04	0.77	93.8	20.0±2.0	0.8	"	0.95
NGC 2685	S0$_3$(7) pec	-1.0±0.8	-22.64	0.46	38.0	16.0	3.0^b	Ursa Major South Spur	0.13
NGC 2974	E4	-4.2±1.2	-25.42	0.38	44.0	21.5±2.2	0.7^c	Lynx Cloud	0.26
NGC 3818	E5	-4.6±0.8	-23.94	0.37	95.9	36.3±3.6	...	Crater Cloud	0.20
NGC 3962	E1	-4.8±0.4	-25.07	0.28	10.0	35.3±3.5	2.8^d	"	0.32
NGC 7192	S0$_2$(0)	-3.9±0.7	-24.37	0.05	9.9	37.8±3.8	< 0.7^d	Pavo Indus Spur	0.28
IC 2006	E1	-4.2±0.9	-23.04	0.17	34.8	20.2±2.0	0.3	Fornax Eridanus Cloud	0.82

The morphology (col. 2) is from the Sandage & Tammann (1987) catalog. The morphological type, T (col. 3), the ellipticity, ϵ (col. 5), and the position angle, PA (col. 6), are derived from `Hyperleda` (Makarov et al. 2014) with the exclusion of NGC 7192 which is taken from the CGS atlas. The K_s absolute magnitude (col. 4) is from 2MASS. The adopted Distances (col. 7) are derived from the Extragalactic Distance Database (Tully et al. 2009). The HI masses (col. 8) are obtained using the distance in col. 7 and fluxes from `NED` and the following references: ^{a} Ryan-Weber, Webster & Starvely-Smith (2003); ^{b} Józsa et al. (2009); ^{c} Kim et al. (1988); ^{d} Serra & Oosterloo (2010). The Group identification (col. 9) and the local galaxy density, ρ_{xyz} (col. 10), i.e. the density of galaxies brighter than $M_B = -16$ mag, are from Tully (1988).

cleus in the Far-UV (Rampazzo et al. 2007; Marino et al. 2009). This agrees with results from the study of Lick spectroscopic indices by Longhetti et al. (2000) and Annibali et al. (2007), concerning ages within $r_e/8$, i.e. in the nuclear region, and, more recently, from mid-infrared (MIR hereafter) `Spitzer`-IRS spectral analysis within $\approx$2-3 $r_e/8$. This latter highlights, in a large fraction of ETGs, the role of Polycyclic Aromatic Hydrocarbon features (PAHs) as tracers of episodes of star formation with ages in the range between 1 and 2.5 Gyr, with the exact values depending on the metallicity. This look-back time corresponds to a redshift $z \lesssim 0.2$ (Bressan et al. 2006; Kaneda et al. 2008; Vega et al. 2010; Panuzzo et al. 2011; Rampazzo et al. 2013; Nanni et al. 2013).

Furthermore, ETGs can show Far-UV bright extended structures (e.g. rings, arm-like features, tails), sometimes completely distinct in shape from the optical galaxy body, and often associated to HI emission (Jeong 2009; Thilker et al. 2010; Marino et al. 2011c,a; Salim & Rich 2010; Rampazzo et al. 2011; Salim et al. 2012). Simulations suggest that such UV bright ring/arm-like structures can be either a transient product of a major merger (Mazzei et al. 2014a) or can result from the accretion of a small, gas rich companion (Mapelli et al. 2015). Both observations and simulations concur in indicating that *galaxy-scale rejuvenation processes* occur at least in some ETGs, likely fed by either residual or freshly accreted gas.

This paper, the second of a series based on *Swift* (Gehrels et al. 2004; Citterio et al. 1994; Burrows et al. 2005) multi-wavelength (`XRT` + `UVOT`) observations, is dedicated to tracing signatures of recent evolution in nearby ETGs. The sample includes only the eleven galaxies in Trinchieri et al. (2015, Paper I hereafter) observed by *Swift*. Here, we examine the Near-UV (NUV hereafter) galaxy structures revealed by `UVOT`. Galaxies are selected because of the nearly passive stage of evolution of their nuclear region (Rampazzo et al. 2013). Most of these galaxies, which from the spectrum of their nucleus may be considered as templates of *nearly-dead* ETGs, reveal a manifold of bright and peculiar structures in our NUV *Swift*-`UVOT` images (Figure 7 of Paper I). *What does NUV tell us about their story? Is there a common evolutionary framework for these apparently different galaxies?* The comparison between the NUV, tracing recent episodes of star formation, and the optical spatial struc-

tures, mapping older stellar populations, might provide indications about the formation mechanisms of the NUV-bright structures linking recent and past ETGs evolutionary scenarios. The study of the galaxy structures has recently developed through the multi-wavelength comparison of the Sérsic indices derived from the analysis of the luminosity profiles. Vulcani et al. (2014) fitted with a single Sérsic law a set of bands, from u to H, of a low redshift galaxy sample taken from the *Galaxy And Mass Assembly (GAMA)* survey. They examined both late-type galaxies and ETGs, i.e $n < 2.5$ and $n > 2.5$ in their definition. Late-types show an increase of the Sérsic index with the wavelength (see also Kennedy et al. 2016) unlike ETGs for which n is almost constant (see also La Barbera et al. 2010). They concluded that the variation of the Sérsic index with wavelength is connected with the presence of the disk and likely connected to a radial variation of stellar populations and/or dust reddening. We aim to extend to NUV, so far unexplored, such analysis using our *Swift*-`UVOT` data set.

The paper plan is the following. In Section 2 we recall our sample and in Section 3 we described observations and the reduction techniques adopted. Difficulties in an accurate surface brightness analysis of `UVOT` data are reviewed as well as the reduction packages adopted. Results, presented in Section 4, mainly consider the comparison between the NUV and the optical spatial light distribution. The discussion in the light of the literature is given in Section 5. Finally, Section 6 summarizes our results and conclusions.

2. The sample

Table 1 presents the general characteristics of our ETG sample. The Table does not include NGC 1209, present in Paper I, since the galaxy does not have *Swift* observations. All galaxies are ETGs according to their classification of col.s 2 and 3. A transition case between early and later types is NGC 1415 whose classification has, however, a large uncertainty. Their absolute K_s magnitude range (col. 4), $-25.42 \leq M_{K_s} \leq -22.59$, suggests a large interval in the stellar mass and col. 8 indicates that these ETGs are gas rich on average, with HI masses of the order of 10^9 $M_\odot$. Columns 9 and 10 refer to their environmental properties. The range of the local densities, $0.13 \leq \rho_{xyz}$ (gal Mpc^{-3}) ≤ 0.95 is large, but in general they are in a relatively poor environment.

Galaxies affiliated to the Fornax cluster and the Eridanus cloud are peripheral enough that they are located in regions with densities typical of groups. Adopted distances from the Extragalactic Distance Database (Tully et al. 2009), quoted in column 7, have uncertainties of about 10%.

The sample includes only galaxies selected because in their nuclear region, $2\text{-}3\times r_e/8$, their MIR spectral classes range from 2 to 0 (Rampazzo et al. 2013, and references therein). MIR classes (Panuzzo et al. 2011) describe the spectral characteristics of the nuclear regions. The class-2 spectra show atomic and molecular emission lines plus PAHs features with anomalous inter-band ratios; the class 1 spectra show emission lines without PAHs, while class 0 spectra are characterized only by the silicate emission at $\lambda \sim 10\ \mu m$ and the $\lambda \sim 18\ \mu m$ from evolved stars. Bressan et al. (2006) show that class 0 spectra characterize passively evolving nuclei. The sample avoids class 3 spectra. At odds with class 2, class 3 spectra show normal PAHs inter-band ratios, typical of star forming galaxies, like Spirals. The sample does not include also class 4 spectra. These spectra differ from class 2 ones because they are dominated by a hot dust continuum and sometimes show high ionization lines, both signatures indicating the presence of an AGN. Summarizing, the class 2 -1 nuclear spectra of our ETGs are consistent with traces of a past star formation as well as a possible residual AGN activity (see also Vega et al. 2010) while those of class 0 correspond to a passively evolving stellar population.

According to the galaxy morphology, presented for each band in Figure 7 of Paper I, the sample can be divided into two sets. NGC 1366, NGC 1426, NGC 3818, NGC 3962 and NGC 7192 do not show remarkable feature both in the optical nor in the NUV bands. The remaining six ETGs, namely NGC 1415, NGC 1533, NGC 1543, NGC 2685, NGC 2974 and NGC IC 2006, show bright, sometimes peculiar, ring/arm-like features in the NUV filters.

3. Observations and data reduction

UVOT is a 30 cm telescope in the *Swift* platform operating both in imaging and spectroscopy modes (Roming et al. 2005). We observed our ETGs in imaging in all six available filters, $W2$ (λ_0 2030), $M2$ (λ_0 2231), $W1$ (λ_0 2634), U (λ_0 3501), B (λ_0 4329), V (λ_0 5402). Description of the filters, PSFs (FWHM $2\rlap{.}''92$ for $W2$, $2\rlap{.}''45$ for $M2$, $2\rlap{.}''37$ for $W1$, $2\rlap{.}''37$ for U, $2\rlap{.}''19$ for B, $2\rlap{.}''18$ for V), and calibrations are discussed in Breeveld et al. (2010, 2011).

UVOT data obtained in imaging mode with a 2x2 binning, resulting in 1.004"/pixel, were processed using the procedure described in http:// www.swift.ac.uk/analysis/uvot/. We combined all the images taken in the same filter for each galaxy in a single image using UVOTSUM to improve the S/N and to enhance the visibility of NUV features of low surface brightness.

The final data set therefore contains $W2$, $M2$, $W1$, U, B, V images for each galaxy observed with *Swift*, as we discuss below. The final exposure times per image are different since we complied with the request of preserving the lifetime of the filter wheel and we therefore observed as much as possible in the filter-of-the-day. Total exposure times, already given in Table 3 of Paper I, are reported in Table 2 for convenience.

We used the photometric zero points provided by Breeveld et al. (2011) for converting UVOT count rates to the AB magnitude system (Oke 1974): $zp_{W2} = 19.11\pm0.03$, $zp_{M2} = 18.54\pm0.03$, $zp_{W1} = 18.95\pm0.03$, $zp_U = 19.36\pm0.02$, $zp_B = 18.98\pm0.02$ and $zp_V = 17.88\pm0.01$.

UVOT is a photon counting instrument and, as such, is subject to coincidence loss when the throughput is high, whether due to background or source counts, which may result in an undercounting of the flux. This effect is a function of brightness of the source and affects the linearity of the detector. The U, B and V filters are the most affected although coincidence loss can be present also in NUV filters. In case of our binning, Hoversten et al. (2011, and reference therein) calculates that count rates less than 0.028 counts s^{-1} pixel^{-1} are affected by at most 1% due to coincidence loss. We checked the presence of coincidence loss on all our images. As an example we show the count rates of NGC 1543 in the NUV and optical bands in Figure 1. The NUV filters $UVW2$, $UVM2$ and $UVW1$ are almost free from coincidence loss effects. We verified that in $UVW1$, the most affected of the NUV filters, the region is restricted to a few pixels centered on the galaxy nucleus. For instance in the case of NGC 1415 the level of the 0.028 counts s^{-1} pixel^{-1} in the $UVW1$ filter is exceeded in two pixels at the opposite sides of the innermost annulus revealed.

Coincidence loss effects can be corrected in the case of point sources (Poole et al. 2008; Breeveld et al. 2010). For extended sources a correction process has been performed for NGC 4449, a Magellanic-type irregular galaxy with bright star forming regions, by Karczewski et al. (2013). Even though their whole field is affected, the authors calculate that the statistical and systematic uncertainties in their total fluxes amount to $\approx$ 7-9% overall, for the NUV and the optical bands. Based on these results, we decided not to apply any correction for coincidence loss to our optical data.

Table 2. Total exposure times in the UVOT filters

Galaxy Ident.	W2 [s]	M2 [s]	W1 [s]	U [s]	B [s]	V [s]
NGC 1366	13483	11825	3597	8627	1112	1112
NGC 1415	23990	18595	22887	14857	1607	1562
NGC 1426	9924	5744	11179	5765	544	544
NGC 1533	7412	7220	5607	13198	1848	1848
NGC 1543	17414	29743	20155	15133	1922	1575
NGC 2685	7838	6517	6456	783	783	783
NGC 2974	16495	6709	3548	7689	1082	1082
NGC 3818	10616	8497	3296	15392	424	233
NGC 3962	8487	11333	10490	6699	808	792
NGC 7192	6927	15313	6163	6787	987	987
IC 2006	12014	6238	4992	11181	1431	1338

We considered the presence of instrumental scattered light that, in the NUV filters, may cover the whole frame, and of the light scattered from stars (e.g. Hodges-Kluck & Bregman 2014). This latter may produce ghost-images: for particularly bright stars, a ring pattern is produced. The most affected frames by both effects are the $W2$ and $W1$ filters of NGC 1366 (see § 4.4). Our images are the sum of several (dithered and rotated) frames. This sum tends to smooth out large-scale inhomogeneities in the final frame. Our targets, however, cover a limited portion of the $17'\times17'$ of the UVOT field of view. The background, although not homogeneous due to the above factors, can be well evaluated around each object.

Surface photometry has been performed using the ELLIPSE (Jedrzejewski 1987) fitting routine in the STSDAS package of IRAF, increasing the size of the apertures logarithmically. Foreground and background objects have been removed substituting them with the surrounding background using the IRAF task
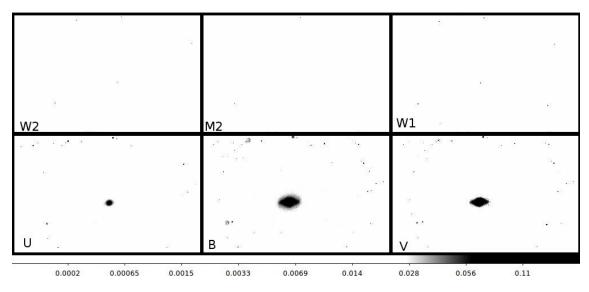
Fig. 1. UVOT count rate images of NGC 1543 by filter (see composite images in Figure 7 for reference). Following Hoversten et al. (2011) non-white areas have a count rate higher than 0.028 counts s^{-1} pixel^{-1} which indicates that coincidence loss effects are larger than 1% in images binned 2×2. U, B, V images appear affected by coincidence loss effects, although at few percent level. At odds, NUV images are unaffected (see text).
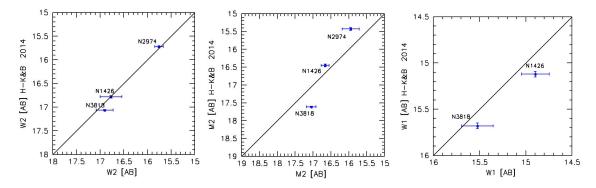

Fig. 2. Our apparent $W2$, $M2$, and $W1$ integrated magnitudes are compared with those derived by Hodges-Kluck & Bregman (2014) (galaxies + halo) for the galaxies in common.

IMEDIT. Ghosts of bright stars remain a serious problem for an accurate surface photometry. Since the problem arises only in the images ($W1$ and $W2$ bands) of NGC 1366, we have masked them in the same way. To secure a reliable background measure, we performed the measurement well beyond the galaxy emission. ELLIPSE provides the semi-major axis lengths (a) the surface brightness (μ), the ellipticity (ϵ), the Position Angle (PA) and the isophotal shape (a_4/a). This term, labeled B_4 in the ELLIPSE table, provides the deviation from the elliptical shape, parametrized by the fourth cosine coefficient of the Fourier expansion of the residuals of the fitting procedure. The sign, the absolute value, and the behaviour of a_4/a are indicative of the boxyness ($a_4/a < 0$) or diskyness ($a_4/a > 0$) of the isophotes (Bender et al. 1989; Capaccioli, Caon & Rampazzo 1990; Governato, Reduzzi & Rampazzo 1993).

From the surface brightness profiles, we derived apparent magnitudes integrating the surface brightness within elliptical isophotes. Errors of the NUV and optical magnitudes where estimated by propagating the statistical errors on the isophotal intensity provided by ELLIPSE. Our NUV and optical integrated magnitudes, reported in Table 3, are not corrected for Galactic extinction. NUV luminosity profiles are provided in Table 4.

Optical UVOT luminosity profiles, in the V band for all galaxies and, additionally, in the U, B bands for NGC 1366, NGC 2685 and NGC 3818, are also reported in Table 4. These profiles will be used to complete the structural analysis of our galaxies (see details in Section 4.3).

4. Results

This section focuses on our main results, i.e. the comparison of our estimated *Swift*-UVOT integrated magnitudes with those available in the literature and the analysis of the NUV surface brightness photometry of our ETGs .

4.1. Integrated magnitudes

In Figure 2 we show the comparison of our integrated NUV magnitudes with those obtained by Hodges-Kluck & Bregman (2014) for NGC 1426, NGC 2974 and NGC 3818. For consistency we corrected our magnitudes for galactic extinction as Hodges-Kluck & Bregman (2014), i.e. following Roming et al. (2009).
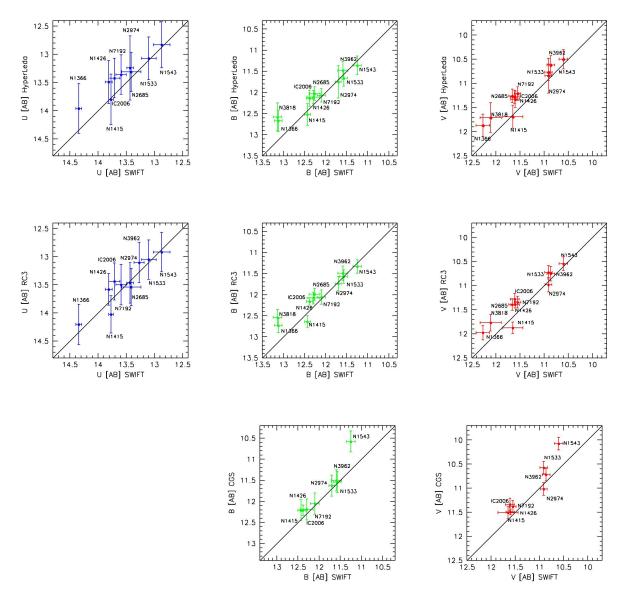
Fig. 3. Comparison between our apparent integrated U, B and V magnitudes and those in the `Hyperleda` (top panels), the RC3 (de Vaucouleurs et al. 1991) (mid panels) and the CGS (Ho et al. 2011; Li et al. 2011) (bottom panels) catalogues, respectively. Magnitudes are in the [AB] system. Error bars of the `Hyperleda` and the RC3 U [AB] magnitudes account for additional ± 0.23 magnitude to include the uncertainty in the conversion from Vega to [AB] magnitudes. Magnitudes are not corrected for Galactic extinction.

Our $W2$ magnitudes are fully consistent with their estimates. Our $W1$ magnitudes are about 1σ brighter. $M2$ values show the largest differences. Our data are almost 2σ fainter than in Hodges-Kluck & Bregman (2014) with the exception of NGC 3818 which is brighter. However, this difference cannot be due to a ghost in our $M2$ images (Trinchieri et al. 2015, their Figure 7) or to the effect of scattered light which is negligible in the $M2$ filter (Hodges-Kluck & Bregman 2014).

We compared our integrated U, B and V magnitudes with the RC3 (de Vaucouleurs et al. 1991) and `Hyperleda`[1] catalogues, after converting their integrated magnitudes in the AB-system applying the following correction AB-Vega: $V = -0.01$, $B = -0.13$, $U = 0.79$. As an additional source of comparison we use the integrated magnitudes provided by the Carnegie-Irvine Galaxy Survey (CGS hereafter, Ho et al. (2011); Li et al. (2011)). This B, V, R, I surface photometric study covers a sig-

nificant fraction of the present sample and has been performed under good seeing conditions. The comparison is shown in Figure 3. Most of our integrated magnitudes are consistent, within errors, with those of the RC3, `Hyperleda`, and the CGS. There are some discrepant cases. Our B and V integrated magnitudes of NGC 1366 and NGC 3818 are fainter than in the RC3 and the `Hyperleda` catalogues. We note that the NGC 1543 B and V integrated magnitude measures in the CGS are discrepant with both the RC3 and the `Hyperleda` magnitudes whose values, in turn, agree with our measures. We estimate that the coincidence loss in the central part of the V profile amounts to 0.1-0.2 mag at most (see Table A2 of Karczewski et al. 2013).

We conclude that our NUV and optical integrated magnitudes in general agree with those literature. The influence of coincidence loss effect in our optical magnitudes are within estimated photometric errors.

---

[1] http://leda.univ-lyon1.fr

Table 3. NUV and optical integrated magnitudes in the AB system

Galaxy	W2	M2	W1	U	B	V
NGC 1366	17.55±0.11	17.39±0.14	16.36±0.07	14.34±0.05	13.12±0.09	12.27±0.14
NGC 1415	15.89±0.07	15.88±0.13	15.00±0.12	13.77±0.04	12.43±0.07	11.65±0.21
NGC 1426	16.89±0.23	16.79±0.11	14.99±0.15	13.81±0.06	12.38±0.07	11.60±0.09
NGC 1533	15.90±0.16	16.07±0.18	14.48±0.08	13.10±0.13	11.57±0.09	10.91±0.08
NGC 1543	15.36±0.22	15.64±0.17	14.28±0.12	12.87±0.15	11.25±0.10	10.60±0.05
NGC 2685	15.53±0.07	15.67±0.13	14.77±0.13	13.41±0.17	12.26±0.13	11.66±0.07
NGC 2974	16.17±0.09	16.40±0.24	15.00±0.15	13.43±0.06	11.70±0.07	10.91±0.07
NGC 3818	17.17±0.18	17.34±0.13	15.73±0.17	14.10±0.15	13.14±0.10	12.11±0.22
NGC 3962	15.90±0.15	16.51±0.11	14.66±0.11	13.27±0.09	11.59±0.12	10.86±0.08
NGC 7192	16.89±0.23	16.79±0.10	15.13±0.17	13.59±0.09	12.10±0.10	11.55±0.07
IC 2066	16.22±0.16	16.37±0.20	15.20±0.18	13.71±0.10	12.29±0.15	11.62±0.09

4.2. The NUV-*Swift* surface photometry

Pictures in the top panels of Figures 4 to 14 compare the optical and the UV morphologies showing color composite multi-wavelength images of our ETGs. Their luminosity profiles in the $W2$, $M2$ and $W1$ bands are plotted in the middle panels of these figures and are tabulated in Table 4, truncated when the uncertainty in the surface brightness exceeds 0.3 mag arcsec^{-2}. As for the integrated magnitudes they are not corrected for galactic extinction.

To parametrize the shape of our NUV luminosity profiles we adopt a Sérsic $r^{1/n}$ law (Sérsic 1968), widely used for elliptical and S0 galaxies since it is a generalization of the $r^{1/4}$ de Vaucouleurs (1948) law (see e.g. Caon, Capaccioli & D'Onofrio 1993). Special cases are $n=1$, the value for an exponential profile, and $n = 0.5$, a Gaussian luminosity profile. Galaxies with n values larger than 1 have a steep luminosity profile in their nuclear regions and extended outskirts. Values smaller than 1 indicate a flat nuclear region and more sharply truncated outskirts. From a 2D luminosity profile decomposition of about 200 ellipticals from the SDSS, Gadotti (2009) measured that the Sérsic index in i-band has a mean value of 3.8 ± 0.9, close to $n = 4$, the historical paradigm for *bona fide* ellipticals (de Vaucouleurs 1948), although with a large scatter.

We best fit a Sérsic law convolved with a PSF, using a custom IDL routine based on the MPFit package (Markwardt et al. 2009), accounting for errors in the surface photometry. The PSF model is a Gaussian of given FWHM and the convolution is computed using FFT on oversampled vectors. We use the nominal value of the FWHM of the PSF for each UVOT filter. However, due to the co-adding, binning and relative rotation of the frames the FWHM is broadened ≈15% from the nominal value (Breeveld et al. 2010). We verified that the effects of the small variations of the PSF are well within the error associated to the Sérsic index. The residuals, $\mu - \mu_{Sersic}$, are shown in the bottom panels of Figures 4 to 14, the Sérsic indices collected in Table 5 and shown in Figure 15.

The structural properties of our galaxies in the NUV bands are collected in Table 5. Columns 2, 3, 4 provide the ellipticity, the position angle (PA) and the isophotal shape parameter, a_4/a, averaged over a_{80} (col. 6) which is the semi-major axis including 80% of the total galaxy luminosity. In this average we exclude the values within $2 \times FWHM_{PSF}$ of the galaxy centers to minimize PSF effects. The quoted error for each measure is the standard deviation around the mean. Figure 16 shows the isophotal shape parameter a_4/a as a function of the semi-major axis in the $M2$ band. Due to the presence of ring/arm-like structures strong

variations are present and motivate our choice to provide the average values of a_4/a, PA and ellipticity, as explained above. Table 5 also reports the Sérsic index resulting from the best fit of the luminosity profile (col. 5) and the notes about the fit (col. 7).

We show in Figure 17 the ($M2$-V) color profiles obtained from our UVOT-$M2$ and V-bands data, i.e. we compare data sets with a similar PSF, avoiding to use the CGS because of the PSF mismatch. We choose the $M2$ band over $W1$ and $W2$ because is less affected by scattered light and ghosts (see § 2).

In the next sub-section, we discuss our NUV photometric results for each single object in the context of the current literature.

4.3. Sérsic index analysis

The study of the Sérsic index is usually performed on "unstructured" ETGs like NGC 1366, NGC 1426, NGC 3818, NGC 3962 and NGC 7192. ETGs with ring/arm-like structures have either knotty, irregular or filamentary morphologies as expected for sites hosting young stellar populations. These features reflect on their luminosity profiles and sometimes they become the dominant characteristics in the NUV luminosity profile. We are however interested in obtaining a description of the galaxy structure underlying these features which may differ when moving from UV to optical bands. For this reason we fit and compare Sérsic indices in different bands considering, case by case, the regions where these features occur (see Section 4.4). This strategy allows us to follow the variation of the underlying galaxy structure, if any, across different wavelengths.

We have decided to use CGS data (Ho et al. 2011; Li et al. 2011) to investigate the variation of the Sérsic index with wavelength for several reasons. All galaxies, except NGC 1366, NGC 2685 and NGC 3818 have B, V, R, I photometry in the CGS, taken with good seeing conditions. They report a median FWHM of the seeing of 1″17, 1″1, 1″01, 0″96 in the B, V, R, I bands, respectively, better than our UVOT B (FWHM=2″18) and V (FWHM=2″19). In few cases the CGS optical luminosity profiles extend further than ours. Finally, the R and I filters allow us to investigate the galaxy photometric structure from NUV to NIR. For NGC 1366, NGC 2685 and NGC 3818, not in the CGS sample, we use our UVOT U, B, V luminosity profiles to complete the analysis of the sample (see Table 4).

To be consistent with our analysis of the UV data, we do not follow multi-component decomposition approaches discussed in the literature such as fitting the profile with multiple Sérsic law profiles by Huang et al. (2013) (see also Laurikainen et al. 2006, 2010, 2011). We performed the analysis of the CGS profiles with a single Sérsic law fit, convolving the profile with the median
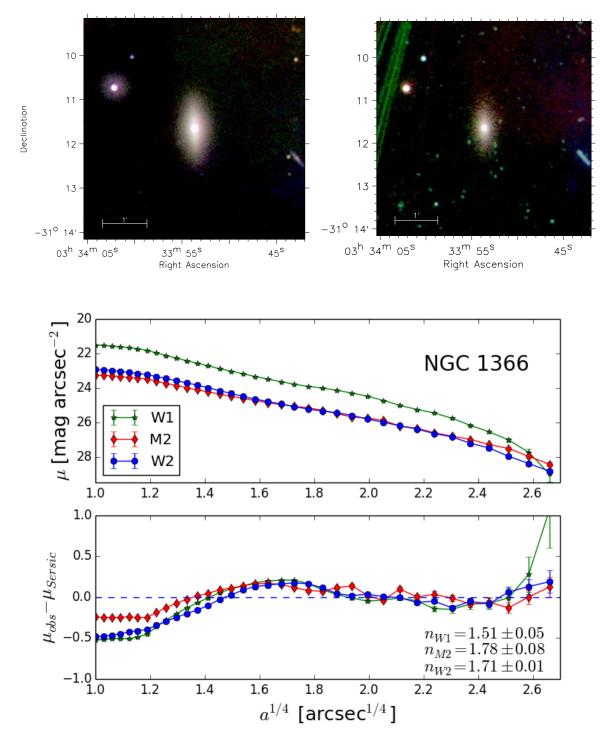
Fig. 4. NGC 1366. Top panels: Color composite image in the U, B, V filters (left: U=blue, B=green, V=red) and W1, M2 and W2 filters (right: W2=blue, M2=green, W1=red). The field of view is 5′×5′, North is on the top, East to the left. Middle and bottom panels: *W1*, *M2* and *W2* luminosity profiles and residuals from their best fit with a single Sérsic law accounting for the filter PSF.

FWHM of the seeing. This choice allows us to use the same criteria adopted for the NUV, i.e. masking the same structures, and extending the fit to the same regions (see notes in column 8 of Table 5) for 9 out of 11 galaxies. For the remaining two galaxies, namely NGC 1533 and NGC 2974, in order to map the underlying galaxy structure we mask the sub-structures present in optical but not in the NUV profiles, or viceversa, as explained in the individual notes of these galaxies.

The synoptic view of the results of the single Sérsic fit for the different bands, from NUV to NIR, is shown in Figure 15. This figure shows that Sérsic indices vary from filter to filter for a given galaxy and also vary from galaxy to galaxy. Few of the indexes plotted comply with the "canonical" value of $n = 4$, highlighted with the arrow in the figure. Before entering in the discussion of these results in the context of the current literature, in the next section we discuss the NUV photometric results in detail for each galaxy.

4.4. Notes on individual galaxies

NGC 1366   A bright star is present to the North. Light scattered by the instrument and a ghost of the star projects in the North-West region around the galaxy in the $W1$ the $W2$ bands. The irregular background could perturb our photometric study in these two bands.

Both the RC3 (de Vaucouleurs et al. 1991) and the RSA (Sandage & Tammann 1987) classify NGC 1366 as an S0. Recently Buta et al. (2015) classified NGC 1366 as SA(rl)0⁻ sp in the survey S⁴G adding the note that a very subtle inner ring-lens (rl) is present (see also Comerón et al. 2014). Our surface photometry extends out to 50″ (∼ 5 kpc using the distance in Table 1), i.e. about $2\times r_{eff}$ in NUV.

The n values (Figure 4 bottom panel) are lower than 2 in all the NUV bands, consistent with the presence of a disk structure. Very similar values are also measured in the U and V bands while the B band gives a larger value of $n = 2.55 \pm 0.03$ (Figure 15). The nuclear part of the galaxy is brighter than the Sérsic model in all the NUV bands.

The a_4/a ratio in $M2$ (Figure 16) shows a boxy nucleus and disky outskirts.

The $(M2 - V)$ color profile of this galaxy (Figure 17) is bluer in the outer parts relative to the inner ones.

NGC 1415   Our photometry extends out to ∼16.5 kpc in radius, $4\times r_{eff}$ on average in our NUV bands. The optical and NUV images (Figure 5, top panels) show the complex structures present in the galaxy which justify its controversial classification: an S0 for the RC3 and a Spiral for the RSA. A complex system of dust is also visible in the optical composite image of the CGS (Ho et al. 2011). More recently, Laurikainen et al. (2011) classified the galaxy as (RL)SABa (r'l,nr)0+ in their Near Infrared Atlas. Buta et al. (2015) assign a morphological type T=-1 adding the notation "grand-design spiral".

In short, recent classifications tend to describe the galaxy as an S0 having an outer ring-lens (RL) system, without bar, with an inner ring-lens (r'l) and a nuclear ring (nr). The system of rings dominates our NUV images, especially in the $M2$ and $W2$ filters, and reflects on the shape of the luminosity profiles: there is not a peak of luminosity in the center since the luminosity of the nuclear ring prevails. The outer ring, well visible in the NUV bands, shows a position angle different from the inner one as pointed out by Comerón et al. (2014). We measure the position angle, PA, and, at the outer edge of the NUV features, the semi-major, a and semi-minor, b, projected axes. The nuclear ring (nr) has PA=166° ± 2°, $a = 10.8″$, $b = 5.2″$; the inner ring-lens (r'l) PA=139° ±2°, $a = 50″$, $b = 14″$; the outer ring (RL) PA=150° ± 2°, $a = 152.8″$, $b = 60.3″$.

The ring/arm-like features perturb the entire NUV luminosity profiles. Without masking any feature, the Sérsic indexes show a large variation $0.85 < n < 2.46$. The range of n values highlights the presence of an underlying disk structure.

The B, V, R, I bands in the CGS cover an area radially more extended than our NUV profiles. The indices summarized in Figure 15 are the result of a fit considering the CGS profile out to the NUV outermost observed radius. Moreover, the fit of the entire CGS profiles provides similar results, comparable within the errors. The Sérsic index ranges from 2.83 ± 0.04 to 3.25 ± 0.38. Values of the Sérsic index $n \geq 3$ argue against a disc morphology in spite of the fact that the galaxy shows a ring revealing the presence of the disk.

The color profile, $(M2 - V)$ in Figure 17 shows strong variations due to the presence of the ring/arm-like structures. The

color is bluer in the inner regions notwithstanding the presence of dust clearly visible in our images, and redder in the outskirts.

NGC 1426   The galaxy is considered a *bona fide* elliptical by both the RC3 and the RSA catalogues. The E classification was questioned by Capaccioli, Piotto & Rampazzo (1988), who studied its geometrical structure down to $\mu_B \approx 28$ mag arcsec⁻². They suggested that NGC 1426 is an S0 since the galaxy does not show any significant isophotal twisting $< PA > = 105° \pm 1°$ out to 100″ (PA=103.5±1.2 in Ho et al. (2011)) as expected for disk galaxies. Huang et al. (2013) model this galaxy with 3 Sérsic components with $n = 2.17, 0.69, 2.13$. There is no comment about a possible galaxy re-classification in their Table 1 on the basis of such low n values. Hopkins et al. (2009) provided a Sérsic fit of the V-band optical profile which combines high resolution inner galaxy regions from *HST* and ground based measurements from different sources. They propose a two component fit, "Sérsic + cusp", with a value of the Sérsic index $5.26^{+0.11}_{-0.35}$ (see their Table 1).

Our integrated NUV magnitudes (Table 5) agree well with those in Hodges-Kluck & Bregman (2014). The bottom panel of Figure 6 shows that our NUV luminosity profiles do not present peculiar features. The range of indexes, obtained with a single Sérsic fit out to $a \sim 90″$, is $2.65 \leq n \leq 2.86$.

The CGS surface photometry extends out to ∼230″, although with large photometric errors in the outskirts, well beyond our NUV data. The value of our Sérsic fit of the CGS data, over the same range as our NUV analysis, outlines values lower than the classic $r^{1/4}$ law, just as in the NUV bands (Figure 15).

The $(M2 - V)$ color profile of this galaxy (Figure 17) is rather flat. The a_4/a isophotal shape profile in the $M2$ band is very noisy in the outskirts, and shows some boxy isophotes in its intermediate part. In the optical Li et al. (2011) show a_4/a (their B_4) consistent with 0 out to 100″.

NGC 1533   In the RSA catalog this galaxy has an uncertain classification, barred S0/Spiral, while it is a barred S0 in the RC3 catalog. The classification of Laurikainen et al. (2011), (RL) SB0°, confirms the RC3 classification, and indicates the presence of an outer ring lens (RL) associated to the barred S0 (Figure 7). Rings are also discussed in Comerón et al. (2014). A Sérsic index value $n = 1.5$ has been obtained by Laurikainen et al. (2006) with a 2D fit of the bulge which they consider as a pseudo-bulge. *GALEX* evidenced a Far UV bright incomplete ring/arm-like feature at a radius of ∼ 45″ − 55″ (see e.g. Marino et al. 2011c, and references therein) with a bright knotty structure. This feature is also visible in our Swift UVOT images. In particular, the top right panel of Figure 7 shows that the UV bright structures are reminiscent of arms. Approximating the edge of the UV bright North-West "arc" with an ellipse having PA=120° ± 2 and semi-major and semi-minor axes $a = 58″$ and $b = 45″$, respectively, we note that this ellipse does not include the UV bright arm-like structure in the South-West. These arm-like structures are predominant features in the NUV luminosity profiles (Figure 7, mid panel).

The single Sérsic fit, shown in Figure 7 (bottom panel), includes the NUV bright structures. We adopt these values of the fit and report them in Table 5 and in Figure 15. The residuals from the fit emphasizes the regions covered by the ring/arm-like features, seen as excesses of light. The nucleus itself shows an excess of light with respect to the fit.

The bar is not as evident in the NUV (see also the a_4/a profile in Figure 16) as it is in the optical bands. In order to map the underlying galaxy structure we decided to mask the CGS B, V, R, I luminosity profiles in the region from 20″ to 90″, corre-

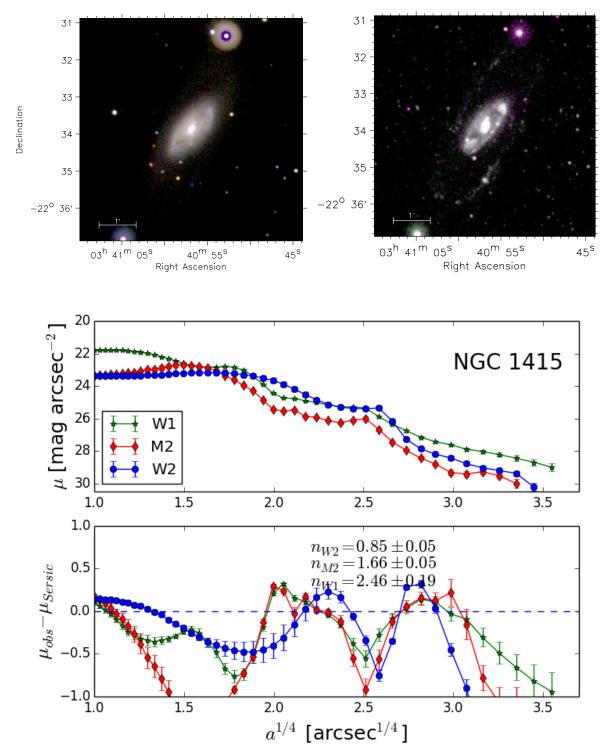**Fig. 5.** As in Figure 4 for NGC 1415. The field of view is 7'×7'. The wide rings around bright sources in the left panel, are an artifact of the UVOT on-board centroid algorithm in the high count rate regime (see also Hoversten et al. 2011, and references therein).

sponding to the bar and the lens, obtaining the n values shown in Figure 15. We test the robustness of the range of the Sérsic index variation repeating the fit of the NUV bands masking the region from 20″ to 90″ as in the optical wavelengths. The Sérsic indices vary from 2.14±0.06 to n=3.69±0.07, in $W2$ and $W1$, respectively, i.e. the values are similar to those in the unmasked NUV fits reported in Figure 7, so we used the unmasked Sérsic fit values for our analysis. Summarizing the values of the Sérsic in-

dex, we select as the best representation of the underlying galaxy structure, range from n ~2.54 ($M2$-band) to 4.89 (V-band).

The ($M2 − V$) color profile (Figure 17) becomes bluer with increasing galactocentric distance beyond 16″. Knots and the arm-like structures discussed above appear bluer than the galaxy body.

NGC 1543 The galaxy, nearly face-on, is classified as a barred S0 both in the RSA and the RC3. Laurikainen et al. (2011) classified the galaxy as (R)SB(l,nl,nb)0+ indicating the presence of

Fig. 6. As in Figure 4 for NGC 1426. The field of view is 5′×5′.

.

a inner lens (l), a nuclear lens (nl), a nuclear bar (nb) in addition to the bar remarked by the RC3 and the RSA, and the outer ring (R). Erwin et al. (2015) decomposed the galaxy luminosity profile with a Sérsic law+exponential, and reported the presence of a disk and of a composite bulge with $n = 1.5$.

The inner and outer bars as well as the lenses are visible in the UVOT optical and NUV images. The outer ring, faint and diffuse in the optical images, becomes brighter in the NUV. Starting from U to $W2$ a filamentary arm-like/ring structure emerges at the outer edge of this ring (Figure 8 top right panel).

The NUV luminosity profiles and the values of Sérsic fit are shown in the bottom panels of Figure 8. We exclude from the single Sérsic fit the ring/arm-like structure in the galaxy outskirts. Notwithstanding, the fit is poor due to the complex structure of the galaxy out to its outskirts (see also the a_4/a profile in Figure 16). The NUV Sérsic indices are lower than 3 and the galaxy nucleus results brighter than the Sérsic model in the NUV filters. In the B, V, R, I bands the Sérsic fit shows that the luminosity profiles are consistent with an $r^{1/4}$ law (Figure 15). The $(M2-V)$ color profile shown in Figure 17 reddens out to 57″
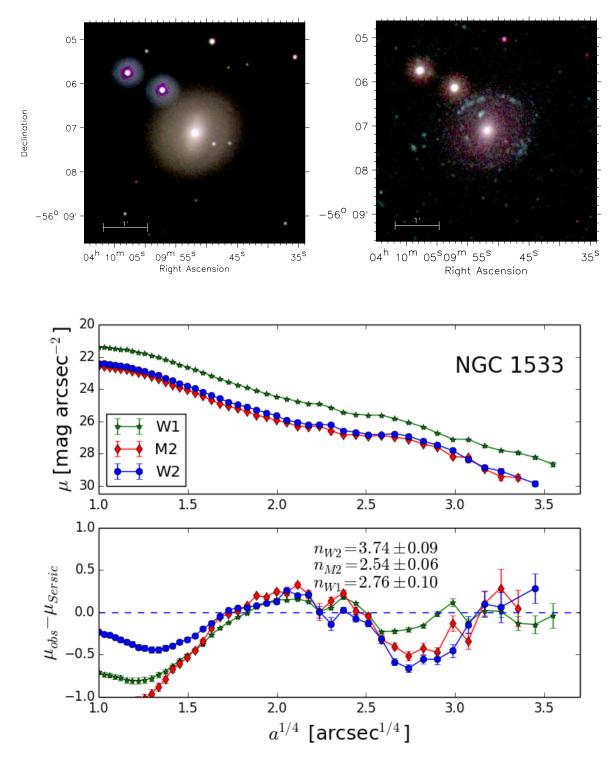
Fig. 7. As in Figure 4 for NGC 1533.The field of view is 5'×5'.

where it starts to become bluer. Colors as blue as $M2 - V \simeq 4$ are found for the arm-like structure at r> 80''.

NGC 2685   The galaxy is known as the "Helix" galaxy. RSA classifies this peculiar object, which shows polar rings and polar dust-lanes, as S0$_3$ pec. Its polar rings/arcs/blobs, well known in the optical bands, become quite spectacular in NUV filters (Figure 9, top right panel).

The NUV emission is very irregular in all UVOT filters. As a consequence, we performed a Sérsic fit to the NUV luminosity profiles without masking any component (see bottom panel of

Figure 9). Since optical luminosity profiles are not available in the literature, we used UVOT U, B and V images to derive luminosity profiles and to estimate the Sérsic indexes, without masking any component as in the NUV. Figure 15 shows the results: all the UVOT bands have very similar values, $n \lesssim 2.5$, suggesting the presence of an extended disk at all wavelengths. A deep optical view of this galaxy is presented by Duc et al. (2015) confirming the picture of an extended low surface brightness disk and ring/arm-like structures (see the top left image in their Figure 17). Therefore, it is no surprising that the $(M2 - V)$ color
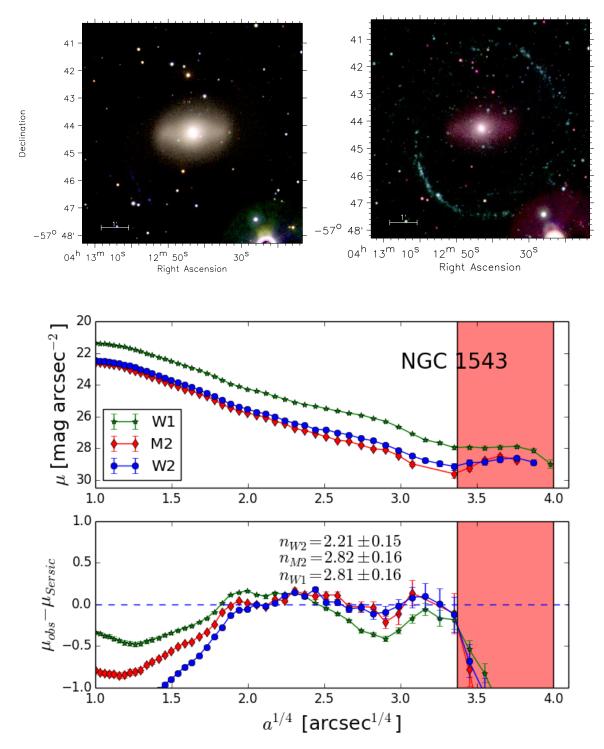
Fig. 8. As in Figure 4 for NGC 1543. The field of view is 8′×8′. The shaded area indicates the masked region in the Sérsic law fit (see text)

of this galaxy becomes bluer, from ∼6 up to ∼2, with increasing galactocentric distance (Figure 17).

NGC 2974   This galaxy is classified as E4 in both the RSA and the RC3. However, Buta et al. (2015) classified it as SA(r)0/a with type T=0.0 A bright star superposed on S-W side of the galaxy hampers the study of this galaxy mainly at optical wavelengths.

The CGS optical image atlas shows the presence of a faint extended ring/arm-like structure in NGC 2974 (Ho et al. 2011; Li et al. 2011). This structure is very bright in the *GALEX* Far-UV

(Jeong 2009; Marino et al. 2011a,b,c) and in our NUV images (top right panel of Figure 10).

The CGS optical and NIR luminosity profiles do not show signatures of this structure which appears in our NUV luminosity profiles. To describe the galaxy underlying structure from NIR to NUV we considered two strategies.
We obtain the NUV Sérsic indices both masking the luminosity profile from 30″ to 100″ where the ring/arm-like features are prominent, and without masking, as in the optical.

In the first case the NUV Sérsic indices derived are very similar to each other, ranging from 3.23±0.15 in the *M*2 band to
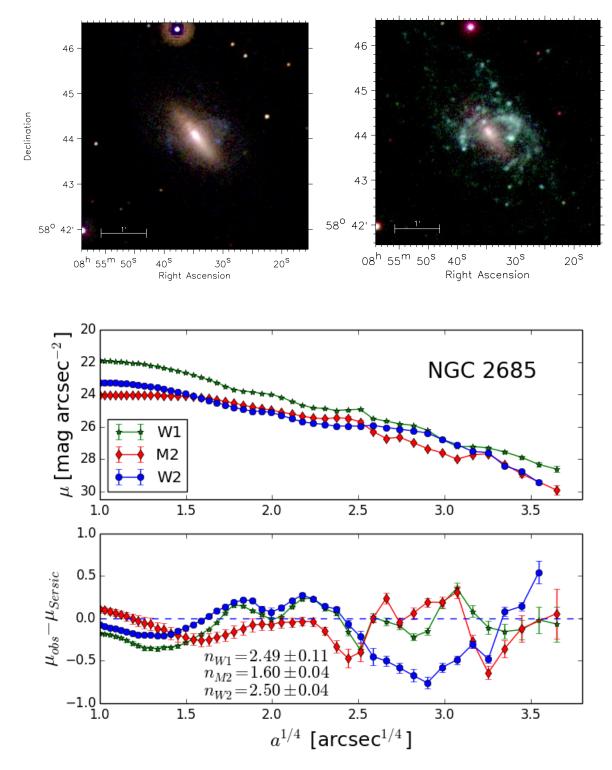
Fig. 9. As in Figure 4 for NGC 2685. The field of view is 5′×5′.

3.43±0.10 in the *W*1 band (these are reported in Figure 10, bottom panel, and in Figure 15). In the second case, i.e. without any masking, we derive $n \lesssim 2.5$ suggesting that the NUV emission marks a disk structure.

The Sérsic indices in NIR and optical bands from the CGS profiles range from 2.9 to 4.2 (see Figure 15). Hopkins et al. (2009), fitting a cusp+Sérsic laws, report a value of the Sérsic index of $4.06^{+0.77}_{-0.48}$ in the V-band.

The blue arm-like structure starts to emerge at $\approx 30''$ in the $(M2 - V)$ color profile of Figure 17.

NGC 3818   This galaxy is classified E5 in the RSA and the RC3. A more detailed description is given by Scorza et al. (1998) that consider NGC 3818 a bulge-dominated ETG, having a disk fully embedded in a boxy bulge.

Our optical images do not show remarkable features (top left panel of Figures 11). The Sérsic index from NUV luminosity profiles is in the range $2.73 \pm 0.18 < n < 3.59 \pm 0.25$. Since
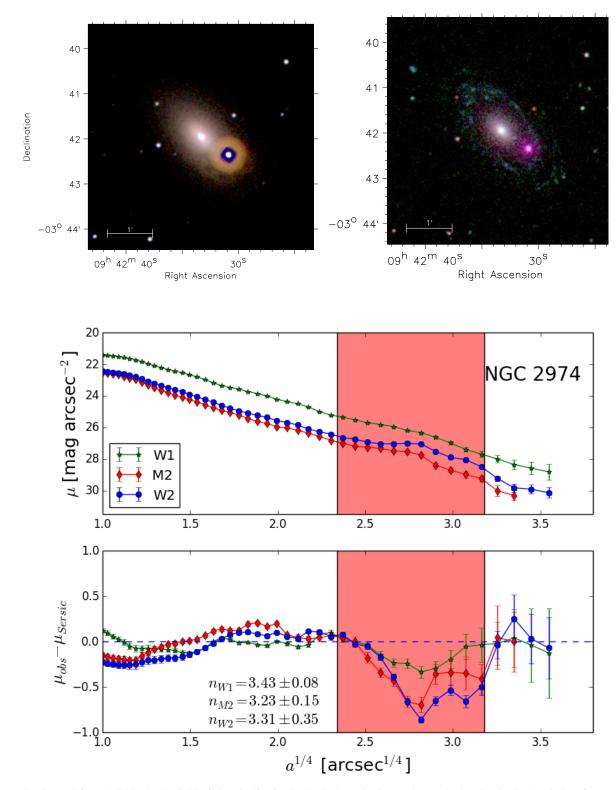
Fig. 10. As in Figure 4 for NGC 2974. The field of view is 5′×5′. The shaded area indicates the masked region in the Sérsic law fit (see text).

the galaxy does not belong to the CGS sample we use our UVOT data-set to study the optical wavelengths.

Our Sérsic index estimate in the UVOT-*V* band is 3.09±0.17 (Figure 15) in agreement with the value of Hopkins et al. (2009), $n = 2.81^{+0.06}_{-0.06}$, in the same band.

We found that the galaxy is slightly disky, as shown in Figure 16 and Table 5. Figure 17 shows that this galaxy has a red color profile, almost constant around an average value, $(M2 - V)\sim5.1$.

NGC 3962   The galaxy is classified E1 in the RSA and the RC3 and E+3-4 by Buta et al. (2015). In the NUV bands we find that its average ellipticity is in the range $\epsilon_{80} \sim 0.18 - 0.24$ (Table 5).

The galaxy does not show an obvious disk structure, although the value of the a_4/a isophotal shape profile tends to
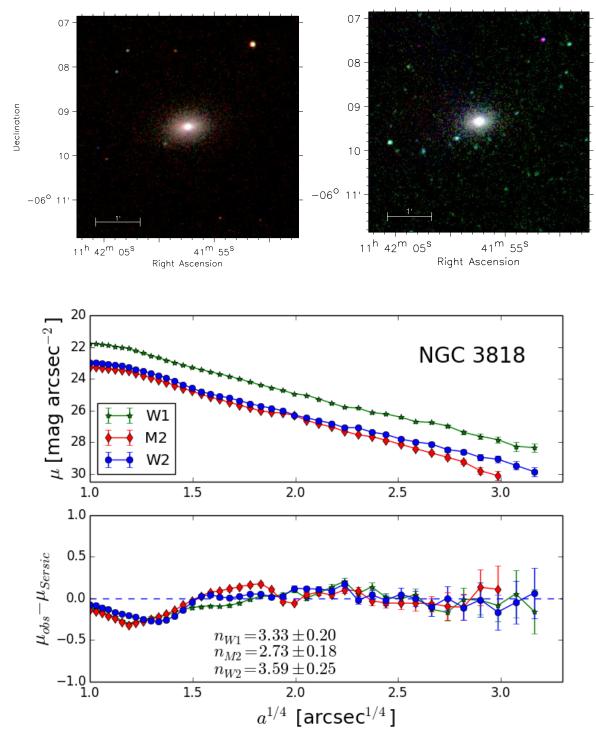
Fig. 11. As in Figure 4 for NGC 3818. The field of view is 5′×5′.

increase towards the outskirts. Furthermore, the NUV luminosity profiles show two distinct trends with a break at $a^{1/4}=2.45$ arcsec$^{1/4}$. This break, visible at the same radius also in the CGS luminosity profiles, is emphasized by our Sérsic fit. Sérsic index values range from 2.52 to 3.28 in the NUV, and from 3.10 to 4.41 in the optical bands (see Figure 15). Huang et al. (2013) find that the V-band profile is well fitted with three Sérsic laws with indexes 3.25, 0.51 and 1.46. The best fit of the sum of a cusp and a Sérsic law in Hopkins et al. (2009) in the same band gives $n = 3.74$. The 2D single Sérsic fit of Salo et al. (2015) is un-

satisfactory ($n = 6.1$) leaving space for a better fit that includes additional components.

Figure 17 shows that this galaxy has a quite red profile, constant around $(M2 − V){\sim}5.3$ out to the galaxy outskirts.

NGC 7192 The galaxy is classified S0 in the RSA and elliptical (.E+..*.) in the RC3. Huang et al. (2013) suggest that the galaxy is an S0 on the basis of a multiple Sérsic fit. Their four component model recognizes a bulge ($n = 1.7$), two lenses ($n=0.4$ and $n=0.5$), and a disk ($n = 0.9$). The presence of two lenses in addition to an outer exponential disk has been previously revealed by Laurikainen et al. (2011). The Huang et al. (2013) model and
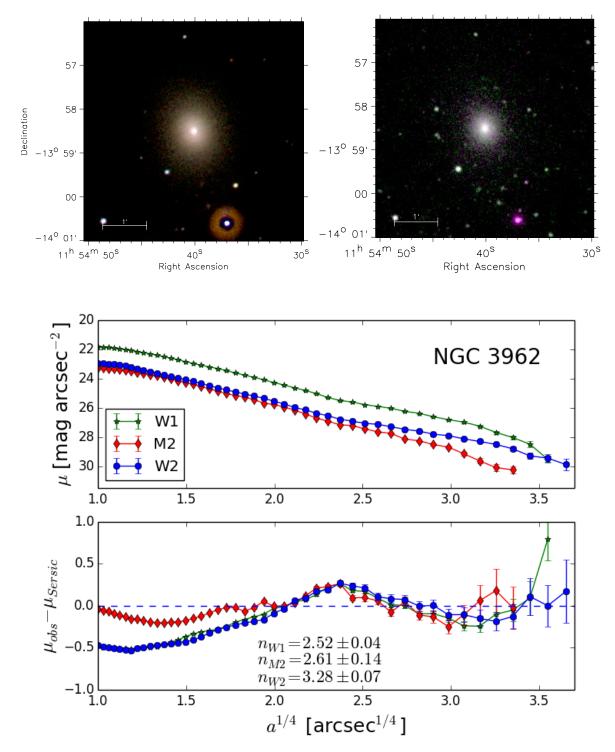
Fig. 12. NGC 3962. As in Figure 4. The field of view is 5′×5′.

that of Laurikainen et al. (2011) converge in indicating that this galaxy is an S0 rather than an E (Huang et al. 2013).

Our fits of the NUV luminosity profiles (Figure 13 bottom panel) provide values of n slightly shallower ($n \approx 3$) than the $r^{1/4}$ law. Similar values are derived in the optical and NIR bands (Figure 15). The nucleus is under-luminous respect to the Sérsic fit both in the $W2$ and $M2$ bands.
We point out that NUV images highlight the presence of a blue knot at 17″5 Nort-West from the galaxy center that does not correspond to any optical feature/star. Possibly, the knot is unre-

lated to the galaxy. The ($M2 - V$) color profile is almost constant around ($M2 - V$)∼5.3 (Figure 17).

IC 2006   The galaxy is classified E1 both in the RSA and Buta et al. (2015), and lenticular with an outer ring (RLA.-..) in the RC3. The B-band deep surface photometry by Schweizer et al. (1989) revealed indeed a faint ring. These authors, however, suggest that the entire profile, including the ring which corresponds to 1-2% of the integrated B-band luminosity, is well approximated by a $r^{1/4}$ law, i.e. the galaxy is a "bona fide" elliptical. Schweizer et al. (1989) found that the ring overlaps with an HI
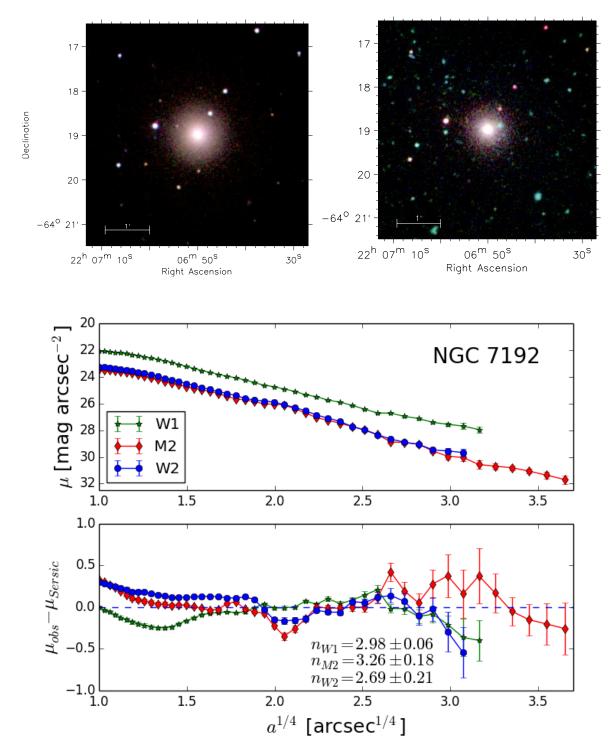
Fig. 13. As in Figure 4 for NGC 7192. The field of view is 5′×5′.

counter-rotating ring at a radius of about 150″, inclined about 37.5°±2° with respect to the plane of the sky.

In our images the outer ring starts to be recognizable in the U-band and becomes more prominent towards $W2$ (Figure 14, top panel). We measure the semi-major and minor axes of the bright UV emission, a=151″, and b=129″, and the PA=40° ± 2°.

The presence of the ring reflects on the NUV luminosity profiles as shown in the bottom panel of Figure 14. In NIR-optical CGS luminosity profiles this feature is not detected. In this context, we decide to exclude the ring, and to fit the Sérsic law of our NUV profiles out to 90″. This produces $n \leq 3.3$ in the NUV bands (bottom panel of Figure 14). Our fit with a single Sérsic law out to 90″ in the B, V, R and I profiles in the CGS gives $n <2.7$ for all of them (Figure 15) and the same values i.e. $n <2.7$ fitting the entire profiles.

Summarizing, Sérsic indices in the range $n \sim 2$ to $n \sim 3.3$ are found from NIR-optical to NUV, as shown in Figure 15. A somewhat larger value, $n = 3.5$, has been recently obtained by Salo et al. (2015) analyzing MIR-images of IC 2006. Our analysis suggests than the ring/arm-like structure should lie on an
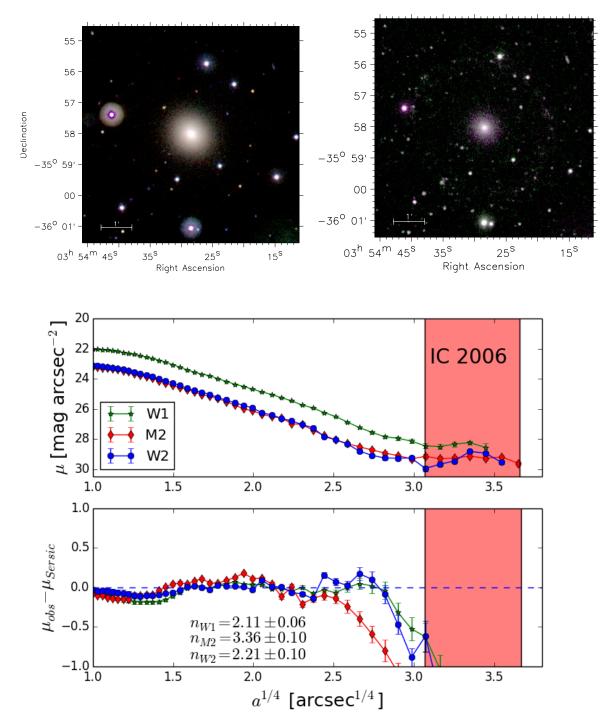
Fig. 14. As in Figure 4 for IC 2006. The field of view is 7′×7′. The shaded area indicates the masked region in the Sérsic law fit (see text).

disk, although the global behavior of the a_4/a does not show a clear evidence of such an underlying feature.

The $(M2-V)$ color profile of this galaxy is constant out to 40-45″(Figure 17) and becomes progressively bluer as the galactocentric distance increases, well before 90″ where the outer bright NUV ring emerges.

5. Discussion

In the introduction we asked two questions: what can our NUV investigation tell us about the history of these ETGs, and whether a common evolutionary framework exists for galaxies showing so different NUV properties. With eleven galaxies only we can-

not present a coherent or exhaustive picture, in particular since we have a variety of behaviors and the properties that apply sometimes to only one of the galaxies and not the others. A more general discussion will have to await for more examples. Nonetheless, we can already see a few common features: the indication that some recent star formation can be detected in the NUV frames, and confirmed by the Sérsic index analysis, suggesting that *wet* accretion could be more common than previously thought even in ETGs. In the following section we connect our NUV results to the multi-wavelength information available in the literature for these galaxies to explore their evolutionary framework.
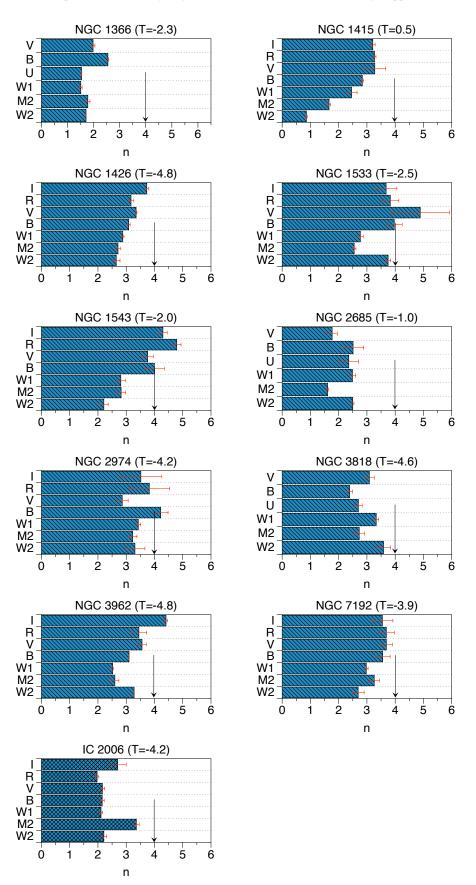
Fig. 15. Synoptic view of the Sérsic indices of the galaxies from NIR to NUV bands. NIR and optical Sérsic indices are obtained from the fit of the luminosity profiles of the CGS (Ho et al. 2011; Li et al. 2011), except for NGC 1366, NGC 2685 and NGC 3818, not included in that catalog. For these galaxies we used UVOT U, B and V bands. The morphological type, T, is taken from Hyperleda as reported in Table 1. The arrows indicate the $r^{1/4}$ law.
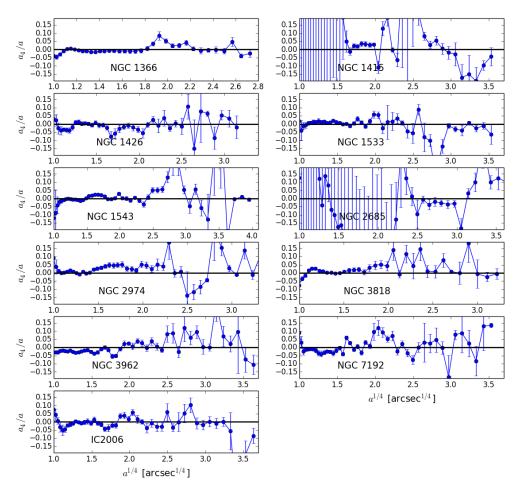
Fig. 16. The isophotal shape, a_4/a, as a function of the semi-major axis in the $M2$ band (see also its average values in Table 5).

5.1. The NUV galaxy structure

Following the multi-wavelength Sérsic index analysis developed in the literature from NIR to u bands (La Barbera et al. 2010; Vulcani et al. 2014; Kennedy et al. 2016) we use our small sample to extend the investigation to the NUV regime.

Figure 15 summarizes the values of the Sérsic indices we derived, from NIR to NUV. As described in the previous section, for each galaxy the fit has been performed with the aim of obtaining the description of the underlying galaxy structure in the different bands. The figure shows that most of the NUV Sérsic indexes are, within errors, in the range 2-3 or lower whereas values corresponding to optical and NIR bands tend to be larger, $n \approx 3 - 4$. Based on the evidence provided by NGC 1366, where a edge-on disk is clearly visible in the NUV images, and all the bands but one have $n < 2$ we can interpret the low n values as evidence of a disk structure in the NUV, as already done at longer wavelengths. Therefore, we can attribute a NUV disk to IC 2006 and NGC 2685.

When comparing the Sérsic index values within each individual galaxy, we notice that variations are less extreme in Es (NGC 2974 and NGC 3818, T< −4). The widest range, consistent with the trend expected for spiral galaxies, is found in NGC 1415, with the "latest" morphology (T=0.5). We therefore, can conclude that, in spite of the small size of the sample, we can reproduce the basic results found in the larger samples in optical and NIR bands: Es, differently from later types, do not show a significant variation in the Sérsic indices with wavelengths (La Barbera et al. 2010; Vulcani et al. 2014; Kennedy et al. 2016).

However, with our extension in the NUV realm, Sérsic indices suggest a disk component in ETGs, likely connected to a recent accretion history and a recent star formation activity.

Do the color profiles indicate the presence of a disk with color bluer than the bulge? Figure 17 shows that there is a large variation in the $(M2-V)$ color profiles of our sample. Four galaxies namely NGC 1426, NGC 3818, NGC 3962, and NGC 7192, have nearly constant colors. For them there is no evidence of a disk that would make the profile bluer with increasing radius. Mazzei et al. (2017, in preparation) will show, in simulating our ETGs, that the color of the younger galaxy populations becomes as red as (M2-V)≈ 5.5 in few 10^8 yr. This behavior, i.e. a global reddening of the galaxy with age, has been found in other bands by Kennedy et al. (2016). They found that both the bulge and the disk become redder with redder total color. We note in addition that the isophotal shape (Figure 16) suggests a disky appearance at the outskirts of both NGC 3818 and NGC 3962.

We notice that the color of NGC 1366, NGC 1533, NGC 1543, NGC 2974 and IC 2006 becomes blue at large radii. The color profile of NGC 1415 is bluer in the intermediate region than it is in the outskirts, likely due to the presence of dust in the outskirts. Only in NGC 2685 the color profile becomes nearly monotonically bluer with radius.

Summarizing, although the Sérsic analysis of NUV luminosity profiles with $n \approx 2 - 3$ suggests the presence of an underlying NUV disk independently of the morphological class and the presence of ring/arm-like structures, the behavior of $(M2-V)$
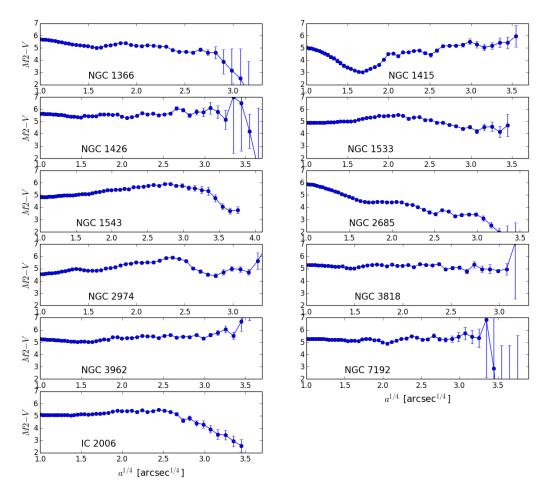
Fig. 17. (*M*2-V) color profiles of our ETGs sample. Profiles are corrected for the galactic extinction following Roming et al. (2009).

color shows a variety of behaviors. Indeed, the color provides less compelling evidence since it can vary rapidly.

5.2. A "wet" evolutionary scenario

The presence of a disk highlighted by our NUV analysis requires a dissipative origin i.e. a recent "wet' galaxy evolution scenario. *Is this scenario supported by other observations? What are the drivers of this evolution?* To address the above questions we choose to investigate SF and kinematical properties dividing ETGs with an unperturbed morphology (NGC 1366, NGC 1426, NGC 3818, NGC 3962 and NGC 7192) from those showing ring/arm-like structures (NGC 1415, NGC 1533, NGC 1543, NGC 2685, NGC 2974 and IC 2006).

In our sample there are several signatures of star formation events even in galaxies with old or relatively old luminosity weighted nuclear ages (e.g. $r_e/8$) (Annibali et al. 2007). Amblard et al. (2014) reported a difference of a factor ≈ 55 between the star formation rate (SFR) of NGC 2685, a polar ring galaxy with the highest star formation rate in our sample (log SFR=-0.36±0.41 $M_\odot$ yr^{-1}), and that of the nearly unperturbed galaxy NGC 1426 (log SFR=-2.08±0.15 $M_\odot$ yr^{-1}). *Spitzer*-IRS observations (Rampazzo et al. 2013) revealed that NGC 1533, NGC 2685, NGC 2974 and NGC 3962 show nuclear PAHs, tracers of some star formation events in the past 1-2.5 Gyr (see e.g. Vega et al. 2010, and references therein).

Concerning evolutionary drivers, there is a *crescendo* of signatures, going from unperturbed morphologies to those char-

acterized by NUV ring/arm-like structures, supporting a "wet" accretion scenario in our ETGs. First of all the fundamental ingredient for a "wet" evolution, the neutral gas, is still abundant. Many of our ETGs own significant HI gas reservoirs (see column 8 in Table 1) that can feed star formation episodes. In addition, kinematical peculiarities point towards interaction/accretion events.

Among ETGs with an unperturbed morfology, NGC 1426 and NGC 3818, do not have indication of accretion episodes. Annibali et al. (2010) report that emission lines in the optical are weak in NGC 3818 and absent NGC 1426, supporting, together with the class 0 of their MIR spectra (Rampazzo et al. 2013), the passively evolving nature of the stellar populations in their nuclear region. Moreover, Annibali et al. (2007) reported an old luminosity weighted age for NGC 1426 (9.0±2.5 Gyr) and for NGC 3818 (8.8±1.2 Gyr) from line-strength indices analysis.

In the remaining ETGs with an unperturbed morphology, namely NGC 1366, NGC 3962 and NGC 7192, signatures of accretion are found. In these galaxies a past star formation episodes may have *rejuvenated* the nucleus (Annibali et al. 2007; Rampazzo et al. 2013).

The nucleus of NGC 1366 has a relatively young luminosity weighted age of 5.9±1.0 Gyr within $r_e/8$ found by Annibali et al. (2010). Morelli et al. (2008) found that NGC 1366 hosts a nuclear kinematically decoupled component younger than the host bulge. To explain the properties of the counter-rotating component, Morelli et al. (2008) suggested that enriched material has been recently acquired via interaction or minor merging.
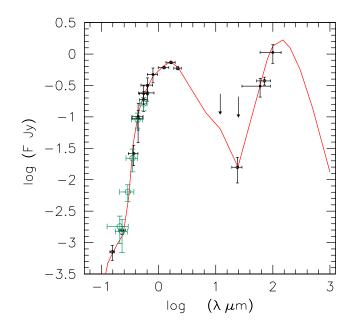
Fig. 18. SED of NGC 1533 with `UVOT`-NUV data (green open circles). The red solid line is the predicted SED, and black open circles and upper limits are observed data as in Mazzei et al. (2014b).

NGC 7192 also has a relatively young nucleus (5.7±2.0 Gyr) (Annibali et al. 2010). Tal et al. (2009) detected a shell system around this galaxy, witnessing its past accretion history. Carollo & Danziger (1994) showed that stars in the innermost 8″ region counter-rotate with respect to stars at larger radii.

NGC 3962 is a particularly intriguing case. The nuclear luminosity weighted age of its stellar populations is 10.0±1.2 Gyr (Annibali et al. 2007). However, the nucleus hosts a radio source (Birkinshaw & Davies 1985; Brown et al. 2011), and recent star formation, since there are PAHs and emission lines (MIR spectral class 2, Rampazzo et al. (2013)). In addition the arm-like structure detected by Buson (1993) in Hα+[NII] supports the presence of a recent/on-going star formation episode (Amblard et al. 2014, report a log SFR=-1.32±0.20 $M_\odot$ yr^{-1}). The NUV and CGS optical luminosity profiles of NGC 3962 show a sudden change of slope at $\approx 35''$. This behavior is remarkably different from the luminosity profiles of the other objects in our sample (see Section 4.4). Two distinct subsystems are also detected by Zeilinger et al. (1996): an inner gaseous disk hosting an old stellar bulge, and an arm-like structure. The inner disk shows regular kinematics with a major axis near PA= 70° and an inclination of about 45° and a radius of about 5″, at the limit of our, better than *GALEX*, resolution. The brighter arm-like feature extends about 20″ corresponding to 3 kpc (Table 1). The Hα+[NII] emission (Zeilinger et al. 1996), however, does not extends out to the region where the change of the slope of the NUV luminosity profile occurs. Neither our `UVOT`-NUV study nor *GALEX* observations (Marino et al. 2011c) show NUV features associated to the Hα emission.

Signatures of "wet" accretion/merging episodes are more evident in ETGs with ring/arm-like structures.

There are no direct signatures of accretion in NGC 1415. The PA of the outer ring (RL), well visible in our NUV images (see Figure 5 top panels), differs from that of the inner ring (r'l) as reported by Comerón et al. (2014). These authors found that the decoupling between the position angles of the inner and outer rings is quite normal among ringed galaxies. However, NGC 1415 is located in the Fornax-Eridanus cloud (Table 1 column

9). Since Eridanus is a loose, irregular, low velocity dispersion group composed of 31 members, many of which spirals (Brough et al. 2006), one cannot discard the hypothesis that the decoupling observed in NGC 1415 may be an effect of the interactions within the group.

NGC 2685, a polar-ring galaxy with gaseous and stellar components dynamically decoupled, is the most striking example for evidence for wet accretion. The outer stars rotate on a polar orbit about a central lenticular galaxy (Whitmore et al. 1990). Ulrich (1975) detected an ionized gas component rotating fast perpendicularly to the galaxy major axis (Schechter & Gunn 1978). The kinematic separation of the two systems is also visible in HI (Józsa et al. 2009, and references therein).

NGC 2974, imaged in Hα, presents some peripheral fainter filaments (Buson et al. 1993) and an ionized disk (Demoulin-Ulrich et al. 1984; Goudfrooij 1994) misaligned with respect to the stellar isophotes by $\approx 20°$(Pizzella et al. 1997). NGC 2974 also has a HI disk (Kim et al. 1988) with the same rotation axis as the stars. Kilborn et al. (2009) revealed HI emission in both NGC 1533 and NGC 1543 (their Figure 4). A detailed map of the very extended HI distribution around NGC 1533 has been provided by Werk et al. (2010). IC 2006 has an HI ring corresponding to the NUV emission as reported above (see Schweizer et al. 1989). The HI is counter-rotating with respect to the stars in the central body of the galaxy. The presence of two peaks of the stellar velocity dispersion map, derived by Scott et al. (2014) with the `WiFes` spectrograph, can be interpreted as a signature of a second counter-rotating component in the inner part of the stellar velocity field.

Our team already explored the formation mechanism and the evolution of ETGs in two nearby groups (Mazzei et al. 2014a) and of some ETGs with ring/arm-like structures simulating, in particular, NGC 1533. We use smooth particle hydrodynamic simulations with chemo-photometric implementation starting from halos of gas and dark matter (Mazzei et al. 2014b) to derive the dynamical and morphological evolution as well as the spectral energy distribution (SED) extending over four orders of magnitude in wavelength at each time. In Figure 18 the `UVOT` integrated magnitudes of NGC 1533, here derived, are overplotted (green open circles) to the predicted galaxy SED (red solid line). The new data agree well with prediction by Mazzei et al. (2014b) and are consistent with their results concerning the evolutionary scenario of this galaxy, that is 13.7 Gyr old according to the simulation, which suggests that NGC 1533 is the product of a wet merger following a 2:1 head-on collision. The UV ring, a transient feature in this galaxy evolution, appears when the galaxy is ≈ 8 Gyr old i.e. in the latter stages of the merger episode.

We conclude that multi-wavelength, kinematical and spectroscopic investigations accumulate in indicating that interaction/accretion/merging episodes have characterized the recent history of many of our galaxies. Many of such episodes left signatures of recent star formation, either in their nuclei and/or in the outskirts. The star formation episodes give evidence that accretions/mergers have been "wet", i.e. that dissipation is the mechanism at the origin of the underlying disk structure revealed by our analysis of NUV luminosity profiles.

6. Summary and conclusion

We present NUV surface photometry of eleven ETGs observed with *Swift*-`UVOT`. These galaxies had their X-ray properties presented in Paper I.

We derive their integrated magnitudes and luminosity profiles in the $W2$, $M2$ and $W1$ NUV bands and as well in optical bands.

We find a variety of behaviors, ranging from the "expected" featureless NUV images in about half of the galaxies examined (NGC 1366, NGC 1426, NGC 3818, NGC 3962 and NGC 7192) to ring-arm/like structures, to evidence of a polar ring (NGC 1415, NGC 1533, NGC 1543, NGC 2974, IC 2006, NGC 2685).

In particular:

- We perform a homogeneous Sérsic analysis of both our NUV and optical data from *Swift* and B, V, R, I luminosity profiles from the CGS finding the following results. For most of our ETGs without and with ring/arm-like structures, regardless the optical classification, Sérsic indices in NUV are on the average in the range $n \approx 2 - 3$ suggesting the presence of an underlying disk. Excluding disk galaxies (e.g. NGC 1366), Sérsic indices from optical profiles are in general larger than those in NUV, being on the average in the range $n \approx 3 - 4$.
- The ($M2$-V) color profiles evidence that the ring/arm-like structures are bluer than the galaxy body suggesting that they host on-going or recent star formation. Featureless ETGs have red colors, however, in NGC 3962 and NGC 3818 the a_4/a isophotal shape is disky in the outskirts. We remind that the color of young stellar populations turns to red ($M2$-V)$\approx$5.5 in a few 10^8 years.

The values of the Sérsic indices in the NUV reveal the role of a dissipative mechanism in these ETGs, which is clearly supported by the presence of residual HI gas. Also NUV unperturbed systems present scars of accretion/merging episodes that "rejuvenated" the galaxy nucleus, as indicated by both their luminosity weighted nuclear ages and PAH observations suggesting star formation episodes in the last few Gyrs. Decoupled gas-stars kinematics further support this view.

We plan to use these far UV data-set, together with the X-ray analysis already presented in Paper I, to constrain a grid of SPH simulations with chemo-photometric implementation providing a self-consistent view of the evolution of our ETGs. In Figure 18 we show how the basic information collected here about their NUV properties will help in defining the SED of NGC 1533 already studied in Mazzei et al. (2014b).

We further emphasized that *Swift*-UVOT data represent an important NUV resource for the study of ETGs in particular for those galaxies which do not have deep *GALEX* images.

Acknowledgments

References

Amblard, A., Riguccini, L., Temi, P., Im, S. Fanelli, M., Serra, P. 2014, ApJ, 783, 135

Annibali, F., Bressan, A., Rampazzo, R., Zeilinger, W. W., Danese, L. 2007, A&A, 463, 455

Annibali, F., Bressan, A., Rampazzo, R., Zeilinger, W. W., Vega, O., Panuzzo, P. 2010, A&A, 519, A40

Bender, R., Surma, P., Döbereiner, S. Möllenhoff C., Madjewsky, R. 1989, A&A, 217, 35

Birkinshaw, M., Davies, R.L. 1985, ApJ 291, 32

Breeveld, A.A., Curran, P.A., Hoversten, E.A, Koch, S., Landsman, W. et al. 2010, MNRAS, 406, 1687

Breeveld, A.A., Landsman, W. Holland, S.T. et al. 2011, in GAMMA RAY BURSTS 2010. AIP Conference Proceedings, 1358, 373

Bressan, A., Panuzzo, P., Buson, L., Clemens, M., Granato, G. L., Rampazzo, R., Silva, L., Valdes, J. R., Vega, O., & Danese L. 2006, ApJ, 639, L55

Brown, M.J.I., Januzzi, B.T., Floyd, D.J.E., Mould, J.R. 2011, ApJL, 731, L41

Brough, S., Forbes, D. A., Kilborn, V. A., Couch, W., Colless, M. 2006, MNRAS, 368, 1351

Burrows, D. N., Hill, J. E., Nousek, J. A., et al. 2005, Space Sci. Rev., 120, 165

Buson, L. 1993, Mem. SAIt, 64, 629

Buson, L., Salder, E., Zeilinger, W., Bertin, G., Bertola, F. et al 1993, A&A, 280, 409

Buta, R.J., Sheth, K., Athanassoula, E. Bosma, A., Knapen J.H. et al. 2015, ApJS, 217, 32

Capaccioli, M., Caon, N. Rampazzo, R. 1990, MNRAS, 242, 24p.

Caon, N., Capaccioli, M., D'Onofrio, M. 1993, MNRAS 265, 1013

Capaccioli, M., Piotto, G., Rampazzo, R. 1988, AJ 96, 487

Comerón, S. Salo, H., Laurikainen, E., Knapen, J.H., Buta, R. et al., 2014, A&A, 562, A121

Carollo, M., Danziger, I.J. 1994, MNRAS 270, 523

Citterio, O., Conconi, P., Ghigo, M., et al. 1994, in SPIE Conf. Ser., ed. R. B. Hoover, & A. B. Walker, 2279, 480

Ulrich-Demoulin M-H., Butcher, H. R., Boksenberg, A., 1984, ApJ, 285, 527

de Vaucouleurs, G. 1948, Ann. Astrophys. , 11, 247

de Vaucouleurs, G., de Vaucouleurs, A., Corwin, H. G., Jr., Buta, R. J., Paturel, G., Fouqué, P. 1991, Third Reference Catalogue of Bright Galaxies. Springer, New York, NY (USA): RC3

Duc, P-A., Cuilllandre, G-C., Karabak, E. Cappellari, M., Alatalo, K. et al. 2015, MNRAS, 446, 120.

Erwin, P., Saglia, R.P., Fabricius, M., Thomas, J., Nowak, N. et al., 2015, MNRAS, 446, 4039

Gadotti, D. A., 2009, MNRAS, 393, 1531

Gehrels, N., Chincarini, G., Giommi, P., et al. 2004, ApJ, 611, 1005

Goudfrooij, P. 1994, Ph.D. thesis, University of Amsterdam, The Netherlands

Governato, F., Reduzzi, L., Rampazzo, R. 1996, MNRAS, 261, 379

Hernández-Pérez, F., Bruzual, G. 2014, MNRAS, 444, 2571

Ho, L.C., Zhao-Yu, L., Barth, A.J. et al. 2011, ApJS, 197, 21: CGS

Hodges-Kluck, E., Bregman, J.N. 2014, AJ, 789, 131

Hopkins, P.F., Cox, T.J., Dutta, S.N., Hernquist, L., Kormedy, J., Lauer, T.R. 2099, ApJS, 181, 135

Hoversten E.A.,Gronwall, C., Vanden Berk, D.E., Basu-Zych, A. R., Breeveld, A. A. et al. 2011, AJ, 141, 205

Huang, S., Ho, L.C., Peng, C.Y., Li, Z-Y., Barth, A.J. 2013, ApJ, 766, 47

Jedrzejewski, R., 1987, MNRAS, 226, 747

Jeong, H., Sukyoung K., Bureau, M., Davies, R.L., Falcón-Barroso, J. et al. 2009, MNRAS, 398, 2028

Józsa, G.I.G., Oosterloo, T.A., Morganti, R. et al. 2009, A&A, 494, 489

Kaneda, H., Honaka, T., Sakon, L. et al. 2008, ApJ, 684, 270

Karczewski, O.Ł., Barlow, M. J., Page, M. J., Kuin, N. P. M., Ferreras, I. et al. 2013, MNRAS, 431, 2493

Kaviraj S., Schawinski, K., Devriendt, J. E. G., Ferreras, I., Khochfar, S. et al., 2007, ApJS, 173, 619

Kennedy, R., Bamford, S.P., Häußler, B., Baldry, I., Bremer, M. et al. 2016, MNRAS, 460, 3458

Kilborn, V. A., Forbes, D. A., Barnes, D. G., Koribalski, B. S., et al. 2009, MNRAS, 400, 1962

Kim, D.-W., Guhathakurta, P., Van Gorkom, J.H. et al. 1988, ApJ 330, 684

La Berbera, F., de Cravalho, R.R., de la Rosa , I.G., Lopes, P.A.A., Kohl-Moreira, L. L., Capelato, H.V. 2010, MNRAS, 408, 1313

Laurikainen, E., Salo, H., Buta, R., Knapen, J., Speltincx, T., Block, D. 2006, AJ, 132, 2634

Laurikainen, E., Salo, H., Buta, R., Kanpen, J.H., Comerón, S. 2010, MNRAS, 405, 1089

Laurikainen, E., Salo, H., Buta, R., Kanpen, J.H. 2011, MNRAS, 418, 1452

Li, Z.-Y., Ho, L. C., Barth, A. J., Peng, C. Y. 2011, ApJS, 197, 22

Longhetti, M., Bressan, A., Chiosi, C., Rampazzo, R. 2000, A&A, 353, 917

Makarov, D., Prugniel, P., Terekhova, N., Courtois, H., Vauglin, I. 2014, A&A, 570, A13

Marino, A., Iodice, E., Tantalo, R., Piovan, L. Bettoni, D. et al. 2009, A&A, 508, 1235

Marino, A., Rampazzo, R., Bianchi, L., Annibali, F., Bressan, A., Buson, L. M., Clemens, M. S., Panuzzo, P., Zeilinger, W. W. 2011a, MNRAS, 411, 311

Marino, A., Bianchi, L., Rampazzo, R., Thilker, D., Annibali, F., Bressan, A., Buson, L. M. 2011b, Ap&SS, 335, 243

Marino, A., Bianchi, L., Rampazzo, R., Thilker, D. A., Annibali, F., Bressan, A., Buson, L. M. 2011c, ApJ, 736, 154

Markwardt, C. B. 2009, Astronomical Data Analysis Software and Systems XVIII, 411, 251

Mapelli, M., Rampazzo, R., Marino, A. 2015, A&A, 575, A16

Martin D. C., Fanson, J., Schiminovich, D., Morrissey, P., Friedman, P. G. et al., 2005, ApJ, 619, L1

Mazzei, P., Marino, A., Rampazzo, R. 2014a, ApJ, 782, 53

Mazzei, P., Marino, A., Rampazzo, R., Galletta, G., Bettoni, D. 2014b, Advances in Space Research, 53, 950.

Morelli, L.; Pompei, E.; Pizzella, A.; Méndez−Abreu, J.; Corsini, E. M.; Coccato, L.; Saglia, R. P.; Sarzi, M.; Bertola, F., 2008, MNRAS 389, 341

Nanni, A., Bressan, A. Marigo, P., Girardi, L. 2013, MNRAS, 434, 2390

Oke 1974, ApJS, 27, 21

Panuzzo, P., Rampazzo, R., Bressan, A., Vega, O., Annibali F., Buson, L.M., Clemens, M.S., Zeilinger, W.W. 2011, A&A, 528, A10

Pizzella, A., Amico, P., Bertola, F. et al. 1997, AA 323, 349

Poole, T. S., Breeveld, A. A., Page, M. J., Landsman, W., Holland, S. T., et al. 2008, MNRAS, 383, 627

Rampazzo, R., Marino, A., Tantalo, R., Bettoni, D., Buson, L.M. et al. 2007, MNRAS, 381, 245

Rampazzo, R., Annibali, F., Marino, A., Bianchi, L., Bressan, A. et al. 2011, Astrphys. Space Scince, 335, 201

Rampazzo, R., Panuzzo, P., Vega , O. et al. 2013, MNRAS, 432, 374

Roming, P.W. A., Kennedy, T. E., Mason, K. O., Nousek, J. A., Ahr, L. et al. 2005, Space Science Rev., 120, 95

Roming, P. W. A., Koch, T. S., Oates, S. R., Porterfield, B. L., Vanden Berk, D. E., et al. 2009, ApJ, 690, 163

Ryan-Weber, E., Webster, R., Starvely-Smith, L.. 2003, MNRAS, 343, 1195

Salim, S., Rich, R.M. 2010, ApJ, 714, L290

Salim, S., Fang, J.J., Rich, R.M., Faber, S.M., Thilker, D.A. 2012, ApJ, 755, 105

Salo, H., Laurikainen, E., Laine, J., Comerón, S., Gadotti, D. A., et al. 2015, ApJS, 219, 4

Sandage, A.R., Tammann, G. 1987, *A Revised Shapley Ames Catalogue of Bright Galaxies*, Carnegie, Washington (RSA)

Schawinski, K., Kaviraj, S., Khochfar, S., Yoon, S.-J., et al. 2007, ApJS, 173, 512

Schechter, P.L., Gunn, J.E. 1978, AJ, 83, 1360

Schweizer, F., van Gorkom, J.H., Seitzer, P. 1989. ApJ 338, 770

Scorza, C., Bender, R., Wilkelmann, C. et al. 1998, A&ASS, 131, 265

Scott, N., Davies, R.L., Houghton, R.C.W., Cappellari, M., Graham, A.W., Pimblet, K.A. 2014, MNRAS, 441, 274

Serra, P., Oosterloo, T.A. 2010, MNRAS, 401, L29

Sérsic, J. L. (ed.) 1968, Atlas de Galaxias Australes (Cordoba, Argentina: Observatorio Astronomico)

Stoughton C., Lupton, R. H.; Bernardi, M., Blanton, M. R., Burles, S. et al., 2002, AJ, 123, 485

Tal, T. van Dokkum, P.G., Nelan, J., Bezanson, R. 2009, AJ, 138 1417

Thilker, D.A., Bianchi, L., Schiminovic, D. et al. 2010, ApJ, 714, L171

Trinchieri, G., Rampazzo, R., Mazzei, P. Marino, A., Wolter, A. 2015, MNRAS, 449, 3021

Tully, R. B. 1988, Nearby Galaxy Catalog, Cambridge University Press

Tully, R. B., Rizzi, L., Shaya, E. J. Courtois, H. M., Makarov, D. I., Jacobs, B. A. 2009, AJ, 138, 323

Ulrich, M-H. 1975, PASP, 87, 965

Vega, O., Bressan, A., Panuzzo, P., Rampazzo, R., Clemens, M.S. et al. 2010, ApJ, 721, 1090

Vulcani, B., Bamford, S.P., Haüßler, B., Vika, M., Rojas A. et al. 2014, MNRAS, 441, 1340

Yi S. K., Yoon, S.-J., Kaviraj, S., Deharveng, J.-M., Rich, R. M. et al., 2005, ApJ, 619, L111

Yi S. K., Lee J., Sheen Y.-K., Jeong H., Suh H., Oh K., 2011, ApJS, 195, 22

Werk, J. K., Putman, M. E., Meurer, G. R., Ryan-Weber, E. V., Kehrig, C., et al. 2010, AJ, 139, 279

Whitmore, B.C., Lucas, R.A., McElroy, D.B., Steiman-Cameron, T, Y., Sackett, P. D., Olling, R. P. 1990, AJ, 100, 1489

Wyder, T.K., Martin, D.C., Schiminovich, D., Seibert, M., Budávari, T. et al. 2007, ApJS, 173, 293

Zeilinger, W.W., Pizzella, A., Amico, P., Bertin, G. et al., 1996, AAS 120, 257

Table 4. Luminosity profiles in the NUV and optical UVOT bands

a arcsec	μ_{W2} [mag arcsec^{-2}]	μ_{M2} [mag arcsec^{-2}]	μ_{W1} [mag arcsec^{-2}]	μ_{U} [mag arcsec^{-2}]	μ_{B} [mag arcsec^{-2}]	μ_{V} [mag arcsec^{-2}]
NGC 1366						
1.0	22.93± 0.01	23.25±0.01	21.51 ±0.01	19.69±0.01	18.33±0.01	17.44±0.01
1.1	22.95± 0.01	23.27±0.01	21.54 ±0.01	19.72±0.01	18.37±0.01	17.49±0.01
1.3	22.99± 0.01	23.30±0.01	21.58 ±0.01	19.76±0.01	18.41±0.01	17.53±0.01
1.4	23.04± 0.01	23.34±0.01	21.62 ±0.01	19.81±0.01	18.48±0.01	17.60±0.01
1.6	23.10± 0.01	23.39±0.01	21.66 ±0.01	19.87±0.01	18.56±0.01	17.69±0.01
1.8	23.16± 0.01	23.43±0.01	21.73 ±0.01	19.95±0.01	18.65±0.01	17.78±0.01
2.0	23.23±0.01	23.49±0.01	21.82±0.01	20.05±0.01	18.76±0.01	17.90±0.01
2.2	23.34±0.01	23.61±0.01	21.97±0.01	20.15±0.01	18.90±0.01	18.03±0.01
2.5	23.46±0.01	23.74±0.01	22.12±0.01	20.29±0.01	19.04±0.01	18.17±0.01
2.8	23.58±0.01	23.86±0.01	22.27±0.01	20.44±0.01	19.22±0.01	18.34±0.01
3.2	23.71±0.01	23.99±0.01	22.42±0.01	20.59±0.01	19.41±0.01	18.54±0.01
3.5	23.84±0.01	24.11±0.01	22.57±0.01	20.78 ±0.01	19.62±0.01	18.74±0.01
4.0	23.99±0.01	24.23±0.01	22.72±0.01	20.95±0.01	19.83±0.01	18.94±0.01
4.5	24.16±0.01	24.36±0.01	22.88±0.01	21.14±0.01	20.05±0.01	19.13±0.01
5.0	24.32±0.01	24.48±0.01	23.03±0.01	21.32±0.01	20.23±0.01	19.31±0.01
5.6	24.49±0.01	24.61±0.01	23.18±0.01	21.50±0.01	20.38±0.01	19.48±0.01
6.3	24.65±0.01	24.74±0.01	23.34±0.01	21.65±0.01	20.50±0.01	19.64±0.01
7.1	24.79±0.01	24.86±0.01	23.49±0.01	21.80±0.01	20.63±0.01	19.76±0.01
7.9	24.94±0.01	24.97±0.01	23.64±0.01	21.90±0.01	20.72±0.01	19.83±0.01
8.9	25.09 ±0.01	25.06±0.01	23.79±0.01	22.00±0.01	20.78±0.01	19.91±0.01
10.0	25.23±0.01	25.16±0.02	23.91±0.01	22.10±0.01	20.86±0.01	20.02±0.01
11.2	25.34±0.01	25.30±0.02	24.01±0.01	22.19±0.01	20.93±0.01	20.13±0.01
12.6	25.44±0.01	25.50±0.02	24.14±0.02	22.31±0.01	20.98±0.01	20.22±0.01
14.1	25.60±0.02	25.69±0.02	24.30±0.02	22.46±0.01	21.10±0.01	20.33±0.01
15.8	25.81±0.02	25.75±0.02	24.48±0.02	22.63±0.01	21.23±0.01	20.49±0.01
17.8	25.99±0.02	25.88±0.02	24.73±0.02	22.84±0.01	21.41±0.01	20.68±0.01
19.9	26.20±0.02	26.22±0.02	25.01±0.03	23.05±0.01	21.61±0.01	20.89±0.01
22.4	26.38±0.02	26.34±0.03	25.25±0.03	23.27±0.01	21.87±0.01	21.10±0.01
25.1	26.65±0.03	26.60±0.03	25.45±0.03	23.51±0.01	22.12±0.01	21.38±0.01
28.2	26.84±0.03	26.80±0.04	25.76±0.05	23.78±0.02	22.43±0.02	21.65±0.01
31.6	27.21±0.04	26.99±0.04	26.17±0.06	24.08±0.02	22.72±0.02	21.97±0.02
35.5	27.49±0.04	27.29±0.05	26.55±0.07	24.42±0.02	23.14±0.02	22.34±0.02
39.8	27.97±0.06	27.52±0.06	27.02±0.11	24.79±0.03	23.52±0.02	22.73±0.03
44.7	28.39±0.09	27.97±0.08	27.74±0.22	25.19±0.04	23.99±0.03	23.09±0.03
50.1	28.83±0.14	28.43±0.12	…	25.62±0.05	24.94±0.07	23.58±0.04
56.2	…	…	…	26.26±0.08	…	24.21±0.01
63.1	…	…	…	26.99±0.16	…	25.18±0.15
NGC 1415						
1.0	23.38±0.01	23.35±0.01	21.79±0.01			18.19±0.02
1.1	23.38±0.01	23.33±0.01	21.79±0.01			18.21±0.02
1.3	23.38±0.01	23.32±0.01	21.79±0.01			18.23±0.02
1.4	23.38±0.01	23.29±0.01	21.80±0.01			18.26±0.02
1.6	23.38±0.01	23.26±0.01	21.80±0.01			18.31±0.02
1.8	23.37±0.01	23.24±0.01	21.80±0.01			18.36±0.02
2.0	23.37±0.02	23.20±0.08	21.81±0.05			18.40±0.02
2.2	23.35±0.02	23.16±0.09	21.87±0.06			18.47±0.02
2.5	23.35±0.03	23.10±0.11	21.91±0.07			18.53±0.02
2.8	23.33±0.03	23.00±0.13	21.99±0.06			18.61±0.02
3.2	23.31±0.03	22.97 ±0.13	22.07±0.06			18.69±0.02
3.5	23.30±0.03	22.89 ±0.14	22.19±0.04			18.80±0.02
4.0	23.26±0.03	22.81 ±0.14	22.31±0.03			18.90±0.02
4.5	23.24±0.03	22.71 ±0.12	22.45±0.02			19.02±0.02
5.0	23.22±0.03	22.70 ±0.11	22.61±0.02			19.15±0.02

Table 4. continued.

5.6	23.19±0.03	22.73 ±0.08	22.75±0.04	19.3±0.02
6.3	23.18±0.04	22.78 ±0.06	22.83±0.05	19.48±0.02
7.1	23.17±0.05	22.88±0.04	22.84±0.06	19.70±0.02
7.9	23.18±0.07	23.06±0.04	22.86±0.06	19.89±0.02
8.9	23.20±0.08	23.35±0.04	22.80±0.06	20.04±0.02
10.0	23.24±0.10	23.63±0.03	22.85±0.07	20.21±0.02
11.2	23.30±0.12	23.95±0.03	23.02±0.07	20.37±0.02
12.6	23.38±0.13	24.29±0.04	23.37±0.06	20.54±0.01
14.1	23.50±0.14	24.84±0.04	23.89±0.05	20.67±0.01
15.8	23.66±0.15	25.43±0.03	24.45±0.03	20.80±0.01
17.8	23.88±0.15	25.55±0.03	24.74±0.02	20.80±0.01
19.9	24.18±0.14	25.47±0.07	24.76±0.04	21.00±0.02
22.4	24.50±0.1	25.87±0.04	24.91±0.03	21.1±0.01
25.1	24.85±0.11	25.93±0.03	25.01±0.02	21.16±0.02
28.2	25.13±0.09	26.13±0.04	25.17±0.02	21.24±0.02
31.6	25.31±0.07	26.27±0.07	25.28±0.04	21.36±0.02
35.5	25.37±0.05	26.10±0.09	25.29±0.07	21.40±0.02
39.8	25.40±0.05	26.01±0.13	25.36±0.10	21.45±0.02
44.7	25.35±0.06	26.67±0.12	25.89±0.07	21.75±0.02
50.1	26.17±0.03	27.44 ±0.08	26.35±0.07	22.15±0.02
56.2	27.28±0.03	27.96 ±0.07	26.75±0.06	22.66±0.03
63.1	27.86±0.05	28.43 ±0.08	27.15±0.05	23.22±0.04
70.8	28.20±0.06	28.80 ±0.01	27.43±0.06	23.43±0.05
79.4	28.42±0.07	29.32 ±0.15	27.61±0.08	23.67±0.07
89.1	28.78±0.10	29.41 ±0.18	27.89±0.09	24.00±0.09
100.0	29.0±0.11	29.27±0.15	28.03±0.11	24.09±0.09
112.2	29.20±0.14	29.51±0.18	28.22±0.13	24.21±0.10
125.9	29.37±0.15	29.99 ±0.269	28.44±0.15	24.44±0.13
141.3	30.20±0.23	. . .	28.69±0.19	24.68±0.15
158.5	. . .	. . .	28.99±0.23	25.03±0.21

Semi-major axis (col. 1), surface brightness and error in $W2$ (col. 2), $M2$ (col. 3) and $W1$ (col. 4). The U (col. 5), B (col. 6) and V (col. 7) bands are not corrected for coincidence loss. (continue.)

Table 5. The NUV structural properties of galaxies

band	$\langle \epsilon \rangle$ [1-b/a]	$\langle PA \rangle$ [deg]	$\langle a_4/a \rangle$ ×100	n	$a_{(80)}$ [arcsec]	Notes
			NGC 1366			
W2	0.40±0.03	1.4±2.4	-4.3±14.3	1.71±0.01	34.7	(1)
M2	0.40±0.09	2.2±1.8	1.4±4.4	1.78±0.08	42.2	(1)
W1	0.47±0.15	179.8±3.7	1.8±3.1	1.51±0.05	23.5	(1)
			NGC 1415			
W2	0.60±0.17	141.2±6.3	-34.9±60.0	2.46±0.19	74.4	(1)
M2	0.33±0.12	143.6±24.8	8.7±36.1	1.66±0.05	57.4	(1)
W1	0.34±0.09	137.1±19.5	0.5±18.2	0.85±0.05	98.2	(1)
			NGC 1426			
W2	0.30±0.05	103.6 ±19.4	0.4±10.3	2.65±0.13	61.7	(1)
M2	0.30±0.04	109.5±18.2	-1.0±9.5	2.71±0.10	82.7	(1)
W1	0.29±0.06	117.7±34.59	-0.5±5.1	2.86±0.04	148.5	(1)
			NGC 1533			
W2	0.22±0.06	160.2±2.5	-3.3±8.0	2.76±0.10	85.5	(1)[a]
M2	0.20±0.07	174.6±12.9	-1.8±7.6	2.54±0.06	85.5	(1)[a]
W1	0.12±0.09	130.7±51.7	0.2±4.3	3.74±0.09	113.7	(1)[a]
			NGC 1543			
W2	0.20±0.09	120.5±40.8	2.8±10.3	2.81±0.16	197.3	(2)
M2	0.15±0.10	130.7±53.5	4.3±13.8	2.82±0.16	187.9	(2)
W1	0.21±0.11	130.4±53.2	2.3±9.0	2.21±0.15	179.0	(2)
			NGC 2685			
W2	0.47±0.02	35.1±1.12	-4.1±27.1	2.50±0.04	102.0	(1)
M2	0.55±0.22	54.6±35.6	-13.7±21.3	1.60±0.04	86.1	(1)
W1	0.44±0.07	39.8±28.8	-0.6±6.6	2.49±0.11	87.2	(1)
			NGC 2974			
W2	0.38±0.06	45.2±2.5	-0.3±7.9	3.31±0.35	82.7	(2)[a]
M2	0.24±0.06	40.6±4.7	3.2±10.4	3.23±0.15	78.8	(2)[a]
W1	0.35±0.04	46.5±4.1	0.6±3.9	3.43±0.08	82.7	(2)[a]
			NGC 3818			
W1	0.33±0.06	108.0±34.1	1.0±5.7	3.59±0.25	58.8	(1)
M2	0.23±0.05	108.2±27.3	2.5±8.8	2.73±0.18	56.0	(1)
W2	0.32±0.06	101.3±32.9	1.3±8.3	3.33±0.20	75.0	(1)
			NGC 3962			

Table 5. continued.

band	$\langle\epsilon\rangle$ [1-b/a]	$\langle PA\rangle$ [deg]	$\langle a_4/a\rangle$ ×100	n	$a_{(80)}$ [arcsec]	Notes
W2	0.24±0.07	15.4±5.0	-2.4±6.0	3.28±0.07	122.2	(1)
M2	0.22±0.02	8.8±2.5	-2.4±1.0	2.61±0.14	75.0	(1)
W1	0.18±0.04	4.5±28.0	-2.9±5.6	2.52±0.04	105.5	(1)
			NGC 7192			
W2	0.09±0.05	15.5±57.8	0.6±6.5	2.69±0.21	50.8	(1)
M2	0.08±0.06	26.6±69.5	1.1±9.2	3.26±0.18	61.7	(1)
W1	0.06±0.03	146.8±80.3	0.3±6.1	2.98±0.06	100.5	(1)
			IC 2006			
W2	0.08±0.03	32.2±29.8	-0.3±4.2	2.21±0.10	137.6	(2)
M2	0.13±0.05	177.4±60.4	-2.5±10.7	3.36±0.10	151.4	(2)
W1	0.07±0.02	58.2±21.0	-0.4±6.4	2.11±0.06	113.8	(2)

The ellipticity (col. 2), the Position Angle (col. 3) and the isophotal shape, $a_4/a \times 100$, (col. 4) are the mean values calculated in the same range of the luminosity profile, excluding the central 2×FWHM$_{PSF}$. The errors correspond to the standard deviation. The Sérsic index of the single fit is given in column 5. The semi-major axis including 80% of the integrated magnitude is given in column 6. Notes: The fit on optical and NIR profiles is made on the same extension as in the NUV profiles. In particular: (1) The single Sérsic law fit is performed without masking. (1)[a] NGC 1533: the Sérsic fit is performed without masking the NUV profile (Figure 7) while in BVRI we mask the region 20″-90″ where the bar and the lens are present. (2) The Sérsic fit excludes the ring in NUV and BVRI profiles as shown in Figure 8 and Figure 14. (2)[a] The NGC 2974 fit in the NUV is performed masking the region from 30″ to 100″(Figure 10) while in BVRI no masking has been applied. See Section 4.4 for details about *B*, *V*, *R*, *I* Sérsic fits.